The structure of SRA and its implications for Human African Trypanosomiasis

Sebastian Zoll[a], Harriet Lane-Serff[a], Shahid Mehmood[b], Jonathan Schneider[a], Carol V. Robinson[b], Mark Carrington[c] and Matthew K. Higgins[a]

[a] Department of Biochemistry, South Parks Road, University of Oxford, OX1 3QU

[b] Physical and Theoretical Chemistry Laboratory, University of Oxford, South 32 Parks, OX1 3QZ, Oxford, UK

[c] Department of Biochemistry, Tennis Court Road, University of Cambridge, CB2 1QW

To whom correspondence should be addressed: matthew.higgins@bioch.ox.ac.uk

The authors declare that no competing interests exist.

Summary paragraph

Only two trypanosome subspecies are able to cause Human African Trypanosomiasis. To establish an infection in human blood, they must overcome the innate immune system by resisting the toxic effects of the trypanolytic factors TLF1 and TLF2[1,2]. These lipoprotein complexes contain an active, pore-forming component, apolipoprotein L1, ApoL1, that causes trypanosome cell death[3]. One of the two human infective subspecies, *Trypanosoma brucei rhodesiense,* differs from non-infective trypanosomes solely by presence of the serum-resistance-associated protein, SRA, which binds directly to ApoL1 and blocks its pore-forming capacity[3-5]. Since this interaction is the single critical event that renders *T. b. rhodesiense* human infective, detailed structural information that allows identification of binding determinants is crucial to understand immune escape of the parasite. Here we present the structure of SRA and reveal the adaptations that occurred as it diverged from other trypanosome surface molecules to neutralise ApoL1. We also present our mapping of residues important for ApoL1 binding, giving molecular insight into this interaction at the heart of human sleeping sickness.

Main Text

TLFs share many components with high-density lipoprotein particles[1] and contain a single pore-forming component, apolipoprotein L1[3]. ApoL1 is sufficient to kill *T. brucei*[3,6] and, when added as a transgene, protects mice from trypanosome infection[7]. ApoL1 forms cationic pores in planar lipid membranes *in vitro*[8,9]. These show low conductance at acidic pH, but increase in conductivity by ~3000-fold when shifted to a pH of 7.3[8], with both low pH 'priming' and the shift to higher pH required for establishment of high conductivity pores[8]. *In vivo*, trafficking of TLFs into the acidic endocytic compartments is necessary for ApoL1 activity[3,10,11], suggesting that cell death is triggered by formation of pores in the lysosome, followed by lysosomal swelling[12]. However, cell death can occur without lysosomal swelling and lysosomal swelling without cell death[13]. As an alternative, two independent models have been proposed which indicate that ApoL1 induces cell death by either pore formation in the plasma membrane[14] or by mitochondrial fenestration, in a process similar to apoptosis[13]. These models suggest that low conductance pores are established in the lysosome or endosome and open as ApoL1 moves to locations of higher pH[8].

SRA is evolutionarily related to the variant surface glycoproteins, VSGs, that form a densely packed coat on the external face of the trypanosome plasma membrane[15]. However, unlike the VSGs, SRA is found predominantly in the endocytic compartments[3,10,16,17] with a small fraction occasionally detected at the flagellar pocket[16]. Resistance to ApoL1-mediated cell death results from direct interaction between SRA and the C-terminus of ApoL1[3,5], which is thought to first occur in the lysosome and to block subsequent formation of ApoL1 pores[3,8]. The interaction between ApoL1 and SRA has been proposed to be mediated by coiled-coil packing[3], or through formation of an SRA:ApoL1 heterodimer that

uses the interface equivalent to that used by VSGs to homodimerise[18]. However, structural data has been lacking to support or contradict these models.

To determine the structure of SRA, we produced various constructs for crystallisation. SRA contains an N-terminal domain (263 residues), a C-terminal domain (118 residues) and a GPI-anchor attachment site, with the N-terminal domain sufficient to bind and inactivate ApoL1[3]. Crystallisation of this domain proved challenging, with weakly diffracting crystals obtained for only one construct (Supplementary Table 1). We therefore generated monoclonal antibodies that bind to SRA (Supplementary Fig. 1) and do not prevent complex formation with ApoL1 (Supplementary Fig. 2) for use as crystallisation chaperones. Crystals of a methylated complex of SRA (residues 33-261) bound to the Fab fragment of G10_3 diffracted to 2.3 Å resolution (Supplementary table 2). Four copies of the SRA:G10_3 complex were present in the asymmetric unit, with SRA molecules as chains A, D, G and J.

The Fab fragments mediate most crystal contacts, with the N-terminal end of SRA protruding unsupported into a solvent channel. This, together with the presence of many flexible linkers, results in a structure with high overall B-factors. Nevertheless, electron density maps were of sufficient quality, with clear side chain positions, to unambiguously build a nearly complete model, in particular for molecule A, as evidence by the real space correlation of the fit of the model to the electron density (Supplementary Fig. 3 and 4). This model contains all residues from the SRA construct, apart from 12 at the N-terminus, 7 at the C-terminus and the glycine-rich loop 3 that links helices 3 and 4 (residues 142-158), each of which are disordered (Fig. 1). Loop 3 and the disordered N-terminus each contain a cysteine predicted to form a disulphide bond but is not observed in the electron density. Molecules D, G, and J adopt the same overall structure but are less completely modelled, due to disorder within the crystal.

The N-terminal domain of SRA adopts an extended, ~75 Å long structure with an asymmetric cross section. The most prominent feature is an anti-parallel coiled-coil formed by helices 1 (residues 46-81) and 2 (residues 85-119). At the membrane distal end this is complemented by shorter helices 3 (residues 130-139) and 4 (residues 160-175), forming a tightly packed four-helical-bundle that is capped by the unstructured loop. At the C-terminal end of SRA the structure significantly widens. Helices 5 (residues 184-193), 6 (residues 195-205), 7 (residues 214-228) and 8 (residues 234-252) form a compact unit that continues into the GPI-anchored C-terminal domain in the full-length protein. This is tethered to the main coiled-coil with a disulphide bond between helix 1 and the loop connecting helices 4 and 5. Helices 7 and 8 of the membrane-proximal region also provide the attachment point for the Fab fragment (Fig. 1c, Supplementary Fig. 1).

A comparison of SRA with other surface proteins reveals the same core structural motif, confirming a common ancestor with a three-helical-bundle fold (Fig. 2)[19]. While the haptoglobin-haemoglobin receptors, HpHbRs[20-22], and the glutamic acid/alanine rich protein, GARP[23], have preserved three helices of similar length, in SRA and VSGs the third of these is partially broken down into

loops. Nevertheless, while the structure support a model in which SRA has derived from a VSG[15], there are pronounced differences. First, SRA has the biggest reduction of the three-helical-bundle fold seen so far, with the longest helices around one third shorter than those of other related trypanosome surface proteins (Fig. 2a). Secondly, apart from the single disordered loop at the N-terminal end, SRA lacks the complex decorations found at the membrane-distal end of the VSGs. Finally, SRA has gained an additional helix (helix 3) that lies across the interface used by VSGs to dimerise (Fig. 2b).

These differences follow from the different role and subcellular localisation of SRA. Immune pressure has caused the complex loops of the surface exposed VSGs to diversify, allowing expression switching and immune evasion[24]. Dimerisation may also be a consequence of cell surface localisation as it reduces the fraction of the protein surface exposed to immune detection. Cell surface receptors must therefore be elongated to reach above this VSG layer[22]. In contrast, SRA binds to ApoL1 in the lysosome where there is no immune pressure to diversify and no VSG coat over which it must reach, allowing a simpler and more compact molecule.

The location of helix 3 of SRA is of particular interest as it packs against the coiled-coil of helices 1 and 2 and occludes the face of SRA that is equivalent to the dimerisation interface of the VSGs (Fig. 2b). Indeed, SEC-MALLS and small angle X-ray scattering confirm that SRA, and its complex with G10_3 Fab fragment, are monomeric in solution (Fig. 1a, Supplementary Fig. 2, 5 and 6 and Supplementary Table 3) with a crystallographic X-shaped dimer (Supplementary Fig. 7) not observed in solution. This is not compatible with current models of the SRA-ApoL1 interaction as this helix blocks the surface of SRA predicted to make a coiled-coil interaction with ApoL1. We therefore decided to map the ApoL1 binding site on SRA using hydrogen-deuterium exchange mass spectrometry, HDX-MS.

Recombinant ApoL1 was produced in *E. coli* and tested for functionality in trypanosome killing assays (Supplementary Fig. 8). Complexes of SRA and ApoL1 were assembled at pH 4.8 and, after trypsin-digestion, SRA peptides were analysed for protection from deuterium exchange (Fig. 3a, Supplementary Fig. 9). Three regions of SRA showed significantly lower deuterium incorporation in the presence of ApoL1, with the greatest degree of protection for patch PI (residues 62-77) and more limited protection for patches PII (residues 166-172) and PIII (residues 187-201). The absence of global changes in deuterium exchange argues against large-scale ApoL1-induced conformational changes in SRA, but suggest instead that the protected patches identified directly contact ApoL1.

Patch I is located on the C-terminal half of helix 1 and is well resolved in the structure (Supplementary Fig. 3 and 4 and Supplementary table 4). Seven distinct peptides spanned this region, giving insight into deuteration rates, and allowing the patch to be subdivided up into two parts (Fig. 3b). The greatest protection (~80% uptake difference) is in the C-terminal part of patch I. Even after two hours, this area remains almost fully protected from deuteration (Fig.

3c), suggesting that it forms the stable core of the ApoL1 interaction interface. The N-terminal part of patch I, closer to helix 3, is protected at a lower level with ~50% uptake difference. The other two patches with measurable uptake differences are located on the opposite side of the protein, on helices 4 (PII), 5 and 6 (PIII). The difference in exchange for patch II is 20-30% and for patch III is 30-40% suggesting that deuteration is slowed, but not blocked. These patches might make weaker, and more transient, interactions with ApoL1.

To confirm and to further delineate the region of SRA identified as a hot-spot for ApoL1 binding, mutational analysis was used. To prevent disruption of the SRA structure, all buried and structurally relevant residues remained unchanged. Instead, a set of polar, surface exposed residues, N59, K63, S66 and E70, were mutated (Fig. 4a). Residue N59 is located in the slightly less protected part of patch I. A mutation in this residue was combined with one of K63, which lies further down helix 1, in a double mutant (mutA). Both residues were changed to serine to shorten each side chain, but retain its hydrophilic character. Residues S66 and E70, closer to the C-terminal end of helix 1, were mutated to alanine and serine, respectively, and combined in mutB. Both double mutants were further combined into a quadruple mutant, mutAB, to test their additive effect (Fig. 4a). A similar strategy was used to mutate patches II (mutC, residue D171) and III (mutD, residues K193 and E195). All mutants showed identical retention times in size exclusion chromatography (Supplementary fig. 10), and identical spectra and melting temperatures in circular dichroism spectroscopy (Supplementary fig. 11), suggesting no changes in global structure.

The binding of wild-type (wt) and mutant SRAs to ApoL1 was studied at pH 4.8 using microscale thermophoresis (Fig. 4, Supplementary Fig. 12). The binding affinity of SRA for ApoL1 was measured as ~277 nM (Fig. 4b). The K_D values for mutA and mutB were approx. 2.7-fold and 4.4-fold lower, showing that the N-terminal and C-terminal parts of patch I both participate in ApoL1 binding. The K_D for mutAB was ~24 μM, showing a more than 80-fold reduction in ApoL1 binding when compared to wild type SRA (Fig. 4b). In contrast, mutC and mutD showed ApoL1-binding indistinguishable from wild type. The large reduction in affinity for mutAB supports the identification of the stripe of polar residues that comprises patch I as an important part of the binding site for ApoL1. Indeed, an electrostatic component to the interaction between SRA and ApoL1 has been previously proposed as mice expressing ApoL1 variant N388K are completely protected against *T. b. rhodesiense* infections[25] and we found that the N388K mutation of ApoL1 abolished binding to SRA (Supplementary fig. 13).

The principal ApoL1 binding site is therefore the C-terminal half of helix 1 of SRA. Two related models were previously proposed for the SRA:ApoL1 interaction[3,18], neither of which is fully compatible with this finding. An initial model was based on the discovery that mutation of hydrophobic residues located in the N-terminal half of helix 1 of SRA reduced ApoL1 binding, perhaps preventing the formation of a coiled-coil with the C-terminal helix of ApoL1[3]. The structure of SRA reveals that most of the residues mutated in this study are buried and engage in tight knobs-into-holes-packing with residues of neighbouring helix 2 (Fig. 1b). It is therefore likely that reduced ApoL1 binding

resulting from these mutations is due to disruption of the structure of helix 1 and its packing against helix 2 rather than disruption of the ApoL1-binding interface. A second model suggested that the C-terminus of ApoL1 forms a coiled-coil and packs against the coiled-coil of SRA in much the same way that two VSG molecules dimerise[18]. This is also unlikely, as helix 3, which is well resolved in the structure of SRA molecule A, will prevent the formation of a dimerisation-mimicking interface. In addition, this would involve contacts to helix 2, where no protection from deuterium exchange was detected. Finally, in contrast to these earlier models, which propose a hydrophobic interaction, the structure-guided studies presented here show that polar residues form the core of the interface with ApoL1, rendering the interaction electrostatic in nature, supporting previous studies that propose an electrostatic interaction involving the C-terminal peptide of ApoL1 [5,25].

This study leaves two uncertainties about the SRA:ApoL1 interaction. Firstly, in addition to the primary ApoL1 binding site, patches II and III are protected from deuterium uptake in the presence of ApoL1, albeit at significantly lower levels (Fig. 3). It is therefore conceivable that the ApoL1 binding site is complex, and that ApoL1 'wraps' around SRA and contacts these additional sites. Secondly, ApoL1 exists *in vivo* either as part of a TLF particle or associated with a membrane. Since the kinetics of TLF destruction and ApoL1 release are unknown, it is unclear how long ApoL1 remains in solution within the endosomal lumen. It is therefore possible that SRA binds to membrane-associated ApoL1 rather than engaging it in solution[8]. In contrast to this, the studies presented here were conducted in a detergent-containing environment. While the nanomolar affinity observed between ApoL1 and SRA shows that these two components to bind in a stable and specific way in detergent, it is also possible that additional binding interactions occur in a membrane context to complement the interaction identified here. Future structural and functional studies of ApoL1 and SRA in membranes are needed to provide this additional insight. Despite these caveats, this first structure of SRA and the identification of the core of the ApoL1 binding site provide a significant step forwards in understanding the molecular basis for the one critical interaction that allows *T. b. rhodesiense* to cause human sleeping sickness.

Methods

Cloning, Mutagenesis, Expression and Purification of SRA

A DNA-fragment encoding SRA residues 33 to 261 from *Trypanosoma brucei rhodesiense* was codon-optimised for *E. coli* expression (Invitrogen) and cloned into the pET15b expression plasmid (Merck Chemicals). Point mutations were introduced using overlap extension PCR in combination with sequence and ligation independent cloning [26]. Both wt and mutant SRA were expressed as fusion proteins with an N-terminal, thrombin-cleavable hexa-histidine tag in *E. coli* T7 shuffle cells (New England Biolabs) to promote disulphide bond formation in the cytoplasm. After induction of protein expression with 1 mM isopropyl-β-D-thiogalacto-pyranoside (IPTG) the temperature was lowered to

22°C, followed by incubation for a further 12 h. Soluble protein was purified from lysate by nickel-nitrilotriacetic acid (Ni-NTA) affinity-chromatography (Qiagen) followed by buffer exchange into 20 mM Tris (pH 8.0), 500 mM NaCl, and 10 mM imidazole using a HiPrep 26/10 desalting column (GE healthcare). Thrombin mediated tag-cleavage was carried out for 16 h at 22°C. Uncleaved protein as well as the N-terminal cleavage product were removed by passing over Ni-NTA beads. The flow-through, containing un-tagged SRA, was concentrated using an Amicon Ultra centrifugal filter (molecular weight cut-off, 10,000 Da) before size exclusion chromatography (SEC) using a Superdex 75 16/60 and a buffer of 20 mM Hepes (pH 7.5) and 150 mM NaCl.

Cloning, Expression and Purification of ApoL1

A DNA-fragment encoding *Homo sapiens* ApoL1 residues 60 to 398 was codon-optimised for *E. coli* expression (Invitrogen) and cloned into the pET15b expression plasmid (Merck Chemicals). Expression in *E. coli* BL21(DE3) cells (New England Biolabs) was induced with 1 mM IPTG, after which cultures were grown for 12 h at 37°C. Inclusion bodies were solubilised in 20 mM Tris pH 8.0, 6 M guanidine-HCl, 500 mM NaCl and were purified by Ni-NTA affinity chromatography before the elution fractions were diluted into refolding buffer (20 mM MES pH 6.0, 250 mM NaCl, 0.02% n-Dodecyl-β-D-Maltopyranoside (DDM) (Anatrace). The protein was concentrated on a HisTrap column (GE healthcare) and subjected to SEC using a Superdex 200 16/60 in 20 mM citrate (pH4.8), 150 mM NaCl, 0.02% DDM.

Circlular dicroism

Far-UV circular dicroism (CD) spectroscopy experiments were carried out on a Jasco J-815 spectropolarimeter with a 1 mm path cell. SRA and mutants were measured at a concentration of 0.2 mg/ml in 10 mM Hepes, 150 mM NaF, pH 7.5. Spectra were recorded between 195 and 260 nm wavelength. For each spectrum 4 runs were accumulated at an acquisition speed of 50 nm/min and corrected for buffer absorption.

Production of SRA-binding monoclonal antibodies

Monoclonal antibodies (mAbs) were raised by immunizing female BALB/c mice with SRA in accordance with ethical regulations. Endotoxins were removed using Pierce high capacity endotoxin removal spin columns (Thermo Fisher Scientific). The mice were immunised on day 0 with a subcutaneous injection of 100 µg SRA in complete Freud's adjuvant (Sigma-Aldrich), and on days 21, 42 and 62 with an intra-peritoneal injection of 50 µg SRA in incomplete Freud's adjuvant (Sigma-Aldrich). Spleens were harvested on day 64. Splenocytes were extracted from a single spleen and were fused with Sp2/0 myeloma cells. Hybridoma cells were subsequently selected on semi-solid methylcellulose and grown in 96 well plates using ClonaCell-HY Hybridoma Cloning Kit (Stemcell Technologies). Hybridomas secreting SRA-reactive IgG were identified by ELISA in the first instance and then further verified by surface-plasmon resonance as detailed below. Hybridoma

lines expressing mAbs G10_3 and B7_4 were grown in Dulbecco's modified Eagle's medium (DMEM, Sigma-Aldrich) supplemented with 4 mM L-glutamine (Sigma-Aldrich), 100 U penicillin, 0.1 mg/ml streptomycin (Sigma-Aldrich) and 10% fetal calf serum (Gibco). Cells were then transferred step-wise into serum-free CD Hybridoma medium (Life technologies) and cultured in suspension. The cells were harvested after 14 days and the supernatant, containing secreted IgG were ultra-filtered and exchanged for 20 mM Hepes pH 8.0 using a tangential flow filtration device.

To purify monoclonal antibodies, buffer exchanged supernatants were incubated with Protein A/G agarose beads (Thermo Fisher Scientific). The beads were washed with 20 mM Hepes pH 8.0, 300 mM NaCl and bound mAbs eluted with 100 mM glycine pH 2.5. The eluate was immediately neutralized with 6% (v/v) 1 M Tris pH 9.0 and buffer-exchanged into 20 mM sodium phosphate pH 7.0 and 10 mM EDTA. To prepare Fab fragments, mAbs were concentrated to 20 mg/ml and mixed with immobilized papain (Thermo Fisher Scientific). The cleavage reaction was then performed according to the manufacturer's instructions. Uncleaved antibody as well as Fc fragment was removed from solution by passing samples three times over a Protein A HP column (GE healthcare) with Fab fragments in the flow through.

Hybridoma heavy and light chain sequencing

For RNA extraction, 1 x 10^6 hybridoma cells were pelleted in a microcentrifuge and the pellet resuspended in 1 ml ice-cold PBS. 1 ml of Trizol (Thermo Fisher Scientific) was added and the reaction tube incubated for 5 min at 22°C. 250 µl of chloroform was added and the tube shaken vigorously for 15 seconds. Following 5 min incubation time, the tube was centrifuged for another 5 min at 10,000 x g. The aqueous phase was removed and gently mixed with 550 µl isopropanol. RNA was precipitated for 5 min at 22°C and was pelleted by centrifugation at 17,000 x g for 30 min. The isopropanol was removed, and the pellet was washed with 1 ml 75% (v/v) ethanol with 25% DEPC (diethylpyrocarbonate) treated water (Thermo Fisher Scientific) and centrifuged again at 10,000 x g for 5 min. Ethanol was removed and the pellet air-dried before it was taken up in 25 µl DEPC-treated water.

Synthesis of cDNA was performed using Superscript III reverse transcriptase according to manufacturer instructions (Invitrogen). After reverse transcription the cDNA was used as a template for PCR with degenerate primer pairs[27,28] for mouse IgG constant/variable heavy (CH/VH) and constant/variable (CL/VL) regions. PCR was performed with Platinum Taq polymerase (Thermo Fisher Scientific) and the A-overhang used for ligation into the T-overhang plasmid pGEM-T (Promega). Plasmids with appropriate inserts were selected and sequenced.

ELISA

Maxisorp Nunc-Immuno (Thermo Scientific) plates were coated with 50 µl of SRA (10 µg/ml) in carbonate buffer (pH 9.5) by incubation for 16 h at 4°C. The plates were washed six times with 100 µl PBS-T (0.05 % Tween 20 in PBS) and blocked with 200 µl protein-free blocking solution (Thermo Scientific) for 1 h at 22°C. Following another six PBS-T washes, 150 µl hybridoma supernatant was added and the plates were incubated for 2 h at 22°C. The plates were washed again six times with PBS-T and then incubated with 50 µl anti-mouse IgG-Peroxidase (Sigma-Aldrich; 1:5000 in blocking solution) for 1 h at 22°C. After another eight PBS-T and one final PBS wash the plates were developed at 22°C for 15-30 min by adding 100 µl of the substrate TMB (3,3',5,5'-Tetramethylbenzidine; Thermo Fisher Scientific) to each well. The reaction was stopped by addition of 100 µl 2 N H_2SO_4. Absorbance at 450 nm was recorded within 30 min of stopping the reaction using a plate reader.

Surface plasmon resonance

Measurements of the binding of SRA to Fab fragments were performed at 25°C on a BIAcore T200 machine using a buffer of 20 mM Hepes pH 7.5, 150 mM NaCl and a CM5 chip (GE healthcare) coated with protein A/G (PROSPEC). IgG from serum free hybridoma supernatant was coupled to flow path 2 for 120s at 3 µl/min. SRA at 1 µM was flowed over flow path 1 and 2 at 30 µl/min for 240s followed by 600s dissociation time. The chip surface was regenerated with 10 mM glycine pH 1.7 for 120s. Specific binding to immobilized IgG was detected by subtracting the signal obtained on flow path 1 from that on flow path 2.

Crystallization, Data collection and Structure Determination

To form complexes, Fab fragments were mixed with SRA in a 1:2 ratio. Lysine residues were reductively methylated as described [29] and the sample purified using two Superdex 200 16/600 columns in series, and a buffer of 20 mM Tris pH 8.0 and 150 mM NaCl. Successful methylation was assessed by a decrease in SDS-PAGE mobility relative to the un-methylated protein.

Diffraction quality crystals of the SRA:G10_3 Fab complex were obtained using a seeding approach, with seeds obtained from crystals of SRA:B7_4 Fab complex. First, methylated SRA:B7_4 Fab complex was concentrated to 25.7 mg/ml and mixed with 20% w/v PEG 3350, 200 mM calcium chloride (Qiagen) in a 1:1 ratio in a 200 nl drop. Crystals grew in sitting drops after 7 days at 18°C, appearing as clusters of needles. Although these crystals did not diffract sufficiently to allow structure determination, they were used to generate seeds. A few crystals were crushed with micro-tools and sonicated for 1 min in an ultrasonic water bath. Crystals of SRA:G10_3 Fab complex were obtained by mixing 50 nl of SRA:G10_3 Fab at 20.8 mg/ml with 50 nl seed stock and 100 nl of 20 mM sodium formate, 20 mM ammonium acetate, 20 mM sodium citrate tribasic dehydrate, 20 mM sodium potassium tartrate tetrahydrate, 20 mM sodium oxamate, 100 mM tris(base)/Bicine pH 8.5, 20% (v/v) PEG 500 MME and 10 % (w/v) PEG 20,000 (Molecular Dimensions). Plate-like crystals appeared after 4 days at 18°C and were transferred to well solution and flash-cooled in liquid nitrogen.

Diffraction data were collected at the Diamond Light Source beamline I03 (Harwell, United Kingdom) using a Pilatus 6M detector (DECTRIS). Data reduction was performed using XDS [30]. Scattering data from two crystals originating from the same drop were scaled together using XSCALE[30]. The structure was solved by molecular replacement using PHASER[31]. Heavy and light chain of the Fab fragment from pdb entry 4U1G were used as search models. The hypervariable regions were omitted from both chains. Placement of the Fab fragment provided enough phase information to visualize electron density for SRA and manually build a preliminary model using COOT[32]. Crystallographic refinement at 2.3 Å resolution was carried out using PHENIX[33] for simulated annealing and rigid-body refinement and BUSTER/ REFMAC5[34-36] for individual coordinate, B-factor and TLS refinement.

Small-Angle X-Ray Scattering Data Collection and Processing

SAXS data were collected at EMBL Hamburg (Germany), BioSAXS P12 beamline, using a Pilatus 2M detector (DECTRIS) and a wavelength of 1.24 Å at 20°C. For SEC-SAXS, 50µl of SRA:G10_3 Fab at 5 mg/ml were injected onto a Superdex 200 3.2/300 equilibrated in 20 mM Hepes pH 7.5, 150 mM NaCl at a flow rate of 75 µl/min. Scattering data were acquired at one frame per second as components eluted from the column and passed through the SAXS measuring cell. The PRIMUS package[37] was used to normalize the data to the intensity of the incident beam, average frames and subtract scattering contribution from the buffer. In detail, 10 frames corresponding to the void volume of the column were averaged and subtracted from ten averaged frames of the main elution peak.
The radius of gyration, R_g, and forward scattering, $I(0)$; the maximum particle dimension, D_{max} and the distance distribution function, $p(r)$, were evaluated using the program SCÅTTER . The excluded volume of the hydrated particle (the Porod volume, V_p) was computed using the Porod invariant. The particle mass was calculated from the Q_R ratio defined as the volume of correlation square (V_c^2) to R_g [38]. Particle shapes at low resolution were reconstructed *ab initio* by the bead-modeling program DAMMIF[39] using default parameters and evaluated using their normalized spatial discrepancy parameter. The UCSF Chimera package[40] was used for envelope reconstruction at a resolution of 15 Å and automatic fitting of the atomic model.

Microscale Thermophoresis

Microscale thermophoresis measurements were carried out using a Monolith NT.115 (Nanotemper technologies). Experiments were performed at 25°C in premium coated capillaries (Nanotemper technologies). Labelling of ApoL1, which requires detergent for solubility, proved unreliable, and so SRA and its mutants were fluorescently labelled before titrating with increasing concentration of unlabelled full-length ApoL1. Labelling was carried out using AlexaFluor 488 (Thermo Fisher Scientific) at neutral pH. Excess dye was removed and the labelling buffer exchanged for binding buffer of 20 mM citrate

pH 4.8, 150mM NaCl, 0.02% DDM using PD-10 desalting columns (GE Healthcare). Labelled protein was concentrated to 2 μM. ApoL1 was concentrated to 76 μM and mixed with binding buffer in a series of 15 two-fold dilutions. The same amount of SRA was added to each of the dilutions to achieve a final concentration of 1 μM. All dilution series were prepared and measured in triplicates. Following 30 min of incubation at 22°C samples were transferred to capillaries and measurements taken at 100% MST power. Curves were fitted with MO.Affinity Analysis software v2.1.2333 (Nanotemper technologies) using the thermophoretic signal without T-jump (Supplementary figure 10).

Hydrogen-Deuterium exchange mass spectrometry

For Hydrogen-Deuterium exchange mass spectrometry (HDX-MS), gel-filtered SRA and SRA:ApoL1 (1:1.5 molar ratio) were prepared at 80 μM in 20 mM citric acid pH 4.8, 150 mM NaCl and 0.02% DDM. Deuteration was initiated by 15-fold dilution into binding buffer containing D_20. After incubation for 1 min, 45 min and 120 min at 25°C, samples were mixed with 0.5 volumes of pre-chilled quench-buffer of 100 mM Tris(2-carboxyethyl)phosphine (TCEP), 50mM HCl. This lowered the pH to 2.3 and reduced disulphide bonds. After mixing with quench-buffer, samples were frozen in liquid nitrogen. Prior to analysis the samples were thawed quickly and manually loaded.

HDX-MS was performed using a Waters HDX platform composed of a nano-Acquity UPLC coupled to a Synapt G2-Si (Waters) mass spectrometer as previously described[41]. Proteins were digested in-line using a pepsin immobilized column at 20°C. The peptides generated from the pepsin column were trapped on a peptide trap for 2 min for removal of any salts and TCEP at a flow rate of 200 μl min^{-1} and then separated using a C18 column with a linear gradient 5–80% of acetonitrile and water both supplemented with 0.1% formic acid for 12 min at flow rate 40 μl min^{-1}. The temperature of LC was set at 0°C to avoid any back exchange. Sequence coverage and deuterium uptake were analysed using PLGS and DynamX programmes, respectively. Peptide sequence coverage was obtained by using PLGS program and deuterium uptake data was analysed by using DynamX programmes, respectively. Peptide mapping was obtained by using non-deuterated samples in triplicates and only unique peptides present in all three data files were selected for deuterium uptake data analysis. Deuterated sample data was obtained in duplicates for all three deuterium uptake time points. Leucine enkephalin at a continuous flow rate of 5 μl min^{-1} was sprayed as a lock mass for mass correction.

Protein digests provided a list of more than 2000 peptides. After applying several selection filters and manual inspection only 64 peptides were selected for HDX analysis. These peptides provided 100% sequence coverage with many overlapping peptides.

Data availability

Coordinates and structure factors have been deposited in the Protein Data Bank with accession code 6ELU

Correspondence and requests for materials should be addressed to MKH

Acknowledgements

This work was supported by Wellcome Trust grant 093008/Z/10/Z and MRC grant MR/L008246/1. MKH is a Wellcome Trust Investigator. We thank Professor Keith Gull and Dr Sam Dean for assistance with monoclonal antibody generation. We also thank the beamline scientists at Diamond Light Source beamline I03, BioSAXS P12 beamline EMBL Hamburg and Dr David Staunton for assistance with biophysics equipment.

Author contributions

MKH and SZ conceived and designed experiments. MC conducted trypanosome killing experiments. HLS and SZ established protein purification strategies and purified proteins. JS cloned and purified mutant proteins. SM and SZ carried out the HDX experiments. SM and CVR analysed and evaluated the HDX data. SZ collected all X-ray diffraction data (SAXS and crystallography), solved, refined and analysed the structures. SZ carried out the microscale thermophoresis experiments. MKH and SZ wrote the paper with input from co-authors.

References

1. Rifkin, M.R. Identification of the trypanocidal factor in normal human serum: high density lipoprotein. *Proc Natl Acad Sci U S A* **75**, 3450-4 (1978).
2. Tomlinson, S. et al. High-density-lipoprotein-independent killing of Trypanosoma brucei by human serum. *Mol Biochem Parasitol* **70**, 131-8 (1995).
3. Vanhamme, L. et al. Apolipoprotein L-I is the trypanosome lytic factor of human serum. *Nature* **422**, 83-7 (2003).
4. Xong, H.V. et al. A VSG expression site-associated gene confers resistance to human serum in Trypanosoma rhodesiense. *Cell* **95**, 839-46 (1998).
5. Lecordier, L. et al. C-terminal mutants of apolipoprotein L-I efficiently kill both Trypanosoma brucei brucei and Trypanosoma brucei rhodesiense. *PLoS Pathog* **5**, e1000685 (2009).
6. Greene, A.S. & Hajduk, S.L. Trypanosome Lytic Factor-1 Initiates Oxidation-stimulated Osmotic Lysis of Trypanosoma brucei brucei. *J Biol Chem* **291**, 3063-75 (2016).
7. Molina-Portela, M.P., Samanovic, M. & Raper, J. Distinct roles of apolipoprotein components within the trypanosome lytic factor complex

revealed in a novel transgenic mouse model. *J Exp Med* **205**, 1721-8 (2008).
8. Thomson, R. & Finkelstein, A. Human trypanolytic factor APOL1 forms pH-gated cation-selective channels in planar lipid bilayers: relevance to trypanosome lysis. *Proc Natl Acad Sci U S A* **112**, 2894-9 (2015).
9. Molina-Portela Mdel, P., Lugli, E.B., Recio-Pinto, E. & Raper, J. Trypanosome lytic factor, a subclass of high-density lipoprotein, forms cation-selective pores in membranes. *Mol Biochem Parasitol* **144**, 218-26 (2005).
10. Oli, M.W., Cotlin, L.F., Shiflett, A.M. & Hajduk, S.L. Serum resistance-associated protein blocks lysosomal targeting of trypanosome lytic factor in Trypanosoma brucei. *Eukaryot Cell* **5**, 132-9 (2006).
11. Hager, K.M. et al. Endocytosis of a cytotoxic human high density lipoprotein results in disruption of acidic intracellular vesicles and subsequent killing of African trypanosomes. *J Cell Biol* **126**, 155-67 (1994).
12. Perez-Morga, D. et al. Apolipoprotein L-I promotes trypanosome lysis by forming pores in lysosomal membranes. *Science* **309**, 469-72 (2005).
13. Vanwalleghem, G. et al. Coupling of lysosomal and mitochondrial membrane permeabilization in trypanolysis by APOL1. *Nat Commun* **6**, 8078 (2015).
14. Rifkin, M.R. Trypanosoma brucei: biochemical and morphological studies of cytotoxicity caused by normal human serum. *Exp Parasitol* **58**, 81-93 (1984).
15. Campillo, N. & Carrington, M. The origin of the serum resistance associated (SRA) gene and a model of the structure of the SRA polypeptide from Trypanosoma brucei rhodesiense. *Mol Biochem Parasitol* **127**, 79-84 (2003).
16. Stephens, N.A. & Hajduk, S.L. Endosomal localization of the serum resistance-associated protein in African trypanosomes confers human infectivity. *Eukaryot Cell* **10**, 1023-33 (2011).
17. Bart, J.M. et al. Localization of serum resistance-associated protein in Trypanosoma brucei rhodesiense and transgenic Trypanosoma brucei brucei. *Cell Microbiol* **17**, 1523-35 (2015).
18. Pays, E., Vanhollebeke, B., Uzureau, P., Lecordier, L. & Perez-Morga, D. The molecular arms race between African trypanosomes and humans. *Nat Rev Microbiol* **12**, 575-84 (2014).
19. Higgins, M.K. & Carrington, M. Sequence variation and structural conservation allows development of novel function and immune evasion in parasite surface protein families. *Protein Sci* **23**, 354-65 (2014).
20. Stodkilde, K., Torvund-Jensen, M., Moestrup, S.K. & Andersen, C.B. Structural basis for trypanosomal haem acquisition and susceptibility to the host innate immune system. *Nat Commun* **5**, 5487 (2014).
21. Higgins, M.K. et al. Structure of the trypanosome haptoglobin-hemoglobin receptor and implications for nutrient uptake and innate immunity. *Proc Natl Acad Sci U S A* **110**, 1905-10 (2013).
22. Lane-Serff, H., MacGregor, P., Lowe, E.D., Carrington, M. & Higgins, M.K. Structural basis for ligand and innate immunity factor uptake by the trypanosome haptoglobin-haemoglobin receptor. *Elife* **3**, e05553 (2014).

23. Loveless, B.C. et al. Structural characterization and epitope mapping of the glutamic acid/alanine-rich protein from Trypanosoma congolense: defining assembly on the parasite cell surface. *J Biol Chem* **286**, 20658-65 (2011).
24. Metcalf, P., Blum, M., Freymann, D., Turner, M. & Wiley, D.C. Two variant surface glycoproteins of Trypanosoma brucei of different sequence classes have similar 6 A resolution X-ray structures. *Nature* **325**, 84-6 (1987).
25. Thomson, R. et al. Evolution of the primate trypanolytic factor APOL1. *Proc Natl Acad Sci U S A* **111**, E2130-9 (2014).
26. Li, M.Z. & Elledge, S.J. Harnessing homologous recombination in vitro to generate recombinant DNA via SLIC. *Nat Methods* **4**, 251-6 (2007).
27. Wang, Z.D. et al. Universal PCR amplification of mouse immunoglobulin gene variable regions: the design of degenerate primers and an assessment of the effect of DNA polymerase 3 ' to 5 ' exonuclease activity. *Journal of Immunological Methods* **233**, 167-177 (2000).
28. Fields, C. et al. Creation of recombinant antigen-binding molecules derived from hybridomas secreting specific antibodies. *Nat Protoc* **8**, 1125-48 (2013).
29. Walter, T.S. et al. Lysine methylation as a routine rescue strategy for protein crystallization. *Structure* **14**, 1617-1622 (2006).
30. Kabsch, W. Xds. *Acta Crystallogr D Biol Crystallogr* **66**, 125-32 (2010).
31. McCoy, A.J. et al. Phaser crystallographic software. *J Appl Crystallogr* **40**, 658-674 (2007).
32. Emsley, P., Lohkamp, B., Scott, W.G. & Cowtan, K. Features and development of Coot. *Acta Crystallogr D Biol Crystallogr* **66**, 486-501 (2010).
33. Adams, P.D. et al. PHENIX: a comprehensive Python-based system for macromolecular structure solution. *Acta Crystallogr D Biol Crystallogr* **66**, 213-21 (2010).
34. Bricogne G., B.E., Brandl M., Flensburg C., Keller P., Paciorek W., & Roversi P, S.A., Smart O.S., Vonrhein C., Womack T.O. BUSTER version 2.10.1. *Cambridge, United Kingdom: Global Phasing Ltd.* (2016).
35. Winn, M.D. et al. Overview of the CCP4 suite and current developments. *Acta Crystallographica Section D-Biological Crystallography* **67**, 235-242 (2011).
36. Murshudov, G.N., Vagin, A.A. & Dodson, E.J. Refinement of macromolecular structures by the maximum-likelihood method. *Acta Crystallogr D Biol Crystallogr* **53**, 240-55 (1997).
37. Konarev, P.V., Volkov, V.V., Sokolova, A.V., Koch, M.H.J. & Svergun, D.I. PRIMUS: a Windows PC-based system for small-angle scattering data analysis. *Journal of Applied Crystallography* **36**, 1277-1282 (2003).
38. Rambo, R.P. & Tainer, J.A. Accurate assessment of mass, models and resolution by small-angle scattering. *Nature* **496**, 477-+ (2013).
39. Franke, D. & Svergun, D.I. DAMMIF, a program for rapid ab-initio shape determination in small-angle scattering. *J Appl Crystallogr* **42**, 342-346 (2009).

40. Pettersen, E.F. et al. UCSF chimera - A visualization system for exploratory research and analysis. *Journal of Computational Chemistry* **25**, 1605-1612 (2004).
41. Podobnik, M. et al. Crystal structure of an invertebrate cytolysin pore reveals unique properties and mechanism of assembly. *Nat Commun* **7**, 11598 (2016).

Figure Legends:

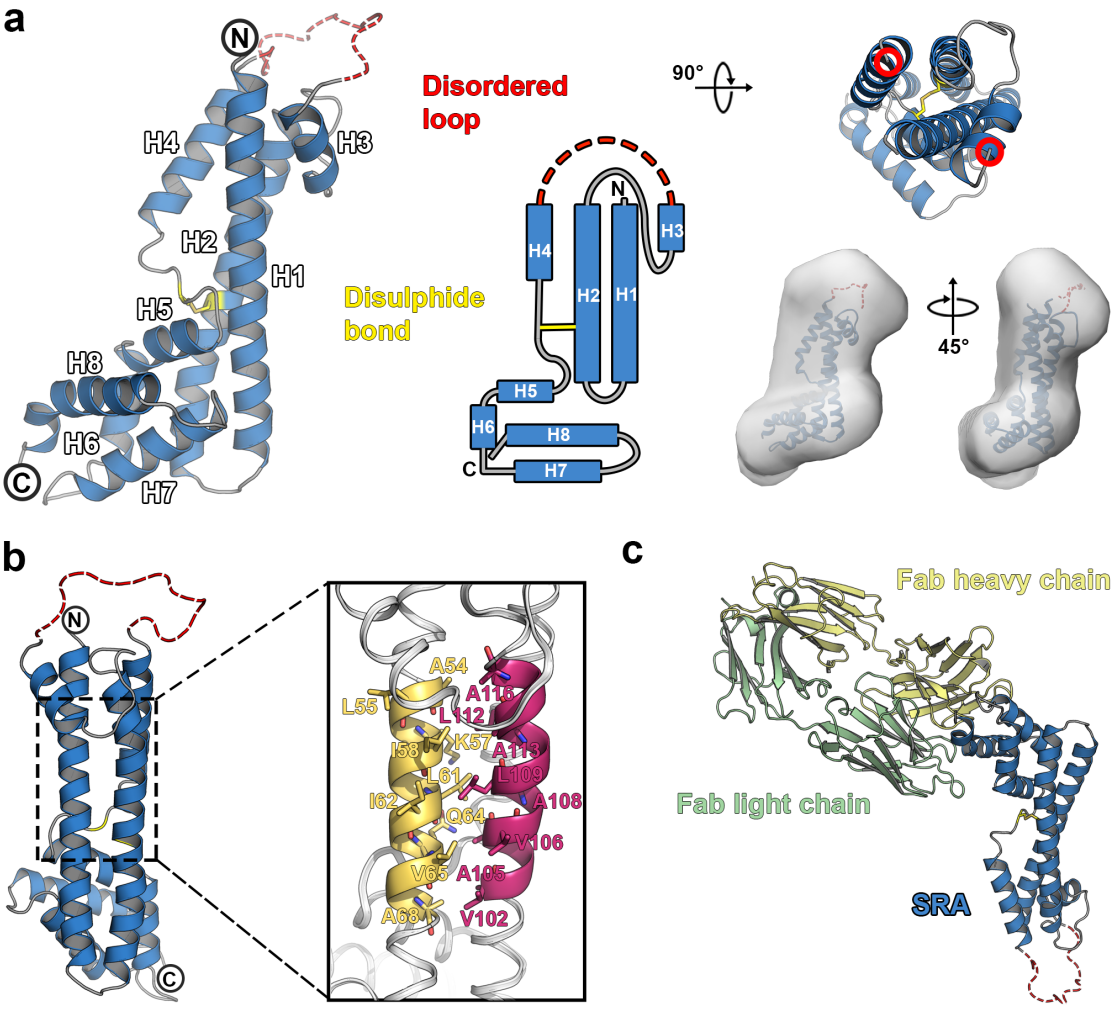

Figure 1. The structure of SRA. a, Two perpendicular views of the crystal structure of SRA are shown, together with a schematic model in which the helices are represented as rectangles. An inset shows two perpendicular views of a molecular envelope derived from SAXS, in which the structure of SRA has been docked. The disordered loop is indicated as dashed lines and is omitted in the top view (right). The N- and C-termini of the loop are indicated with red circles. **b,** Helix 1 and 2 form a coiled-coil. Residues mediating the knobs-into-holes packing that link these helices are highlighted in a close-up view. **c,** Overview of the crystal structure of the SRA:Fab G10_3 complex.

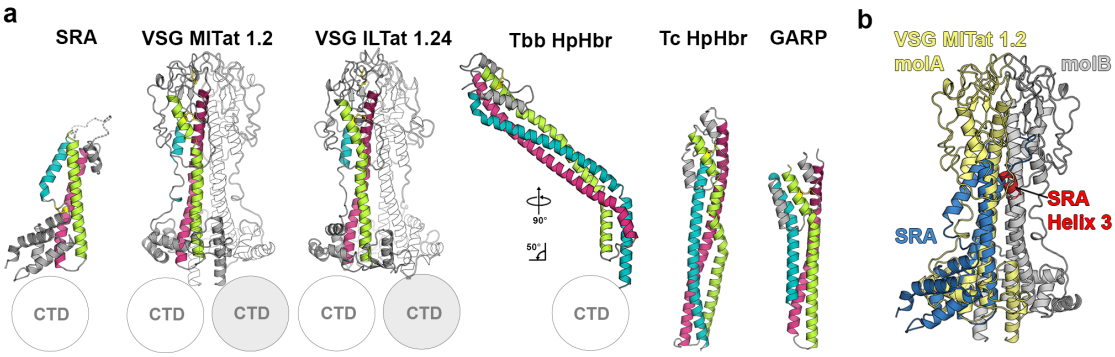

Figure 2. Structural comparison of SRA with known trypanosome surface proteins. a, Structures were aligned using helices 1 (green) and 2 (magenta) and are coloured using the same scheme. For dimeric proteins, one monomer is shown in grey. The positions of the C-terminal domains carrying the GPI-anchor for membrane attachment are estimated by circles. All structures share the same three-helical bundle fold with the third helix (teal) partially broken down in SRA and the VSGs. SRA shows the biggest reduction in length, the lack of elaborate loop-structures in the membrane distal region and **b,** the presence of a small helix (helix 3) that precludes formation of a VSG-like homodimer.

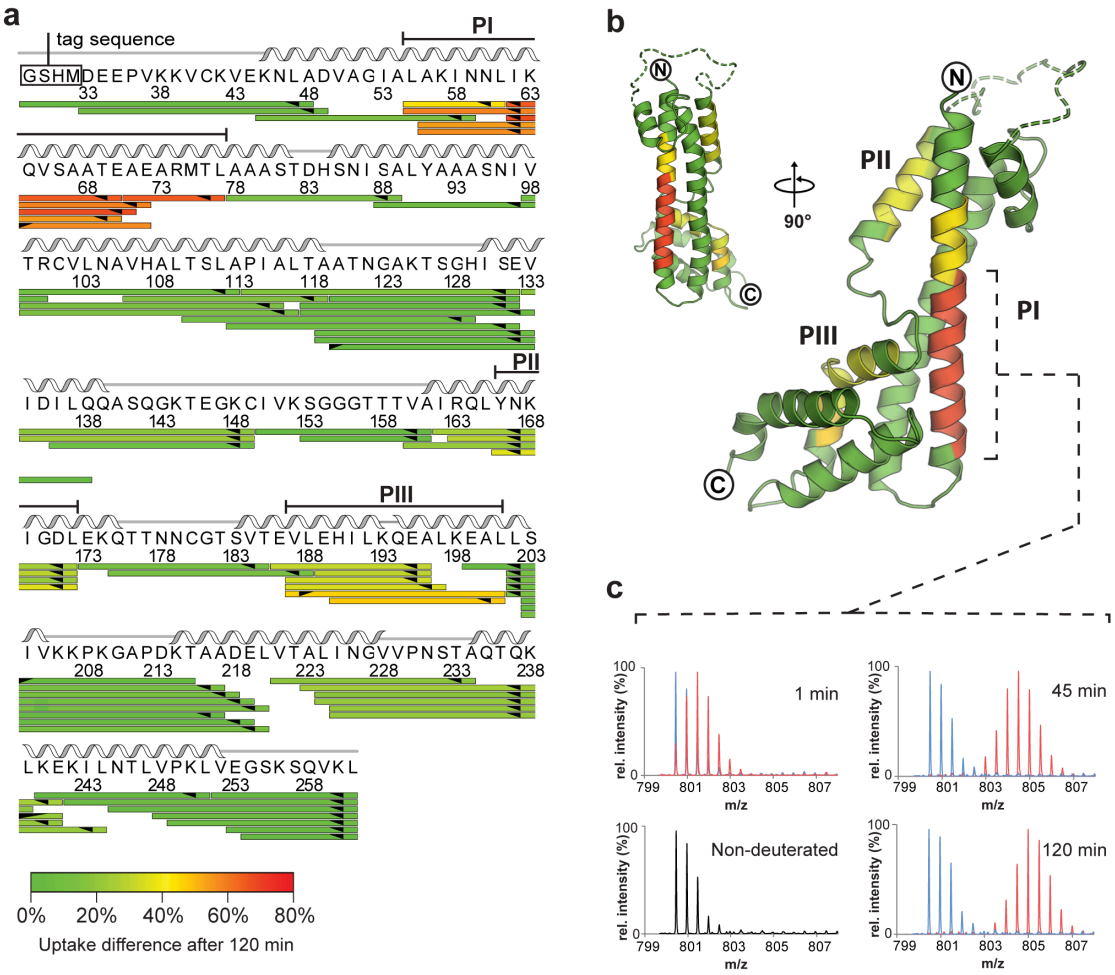

Figure 3. Mapping of the ApoL1 binding site of SRA by hydrogen-deuterium exchange mass-spectrometry. a, The differences in deuterium uptake of SRA and the complex of SRA:ApoL1 mapped on all peptides after 120 min of deuteration. 64 unique peptides were selected, covering 100% of the SRA sequence. The peptides are aligned with the sequence and the secondary structure of SRA. Three points of interaction could be identified (PI, PII, PIII) with the C-terminal part of helix 1 showing the highest difference in deuterium exchange of ~80%. **b,** Exchange differences mapped on the structure of SRA in two views identify the locations of protected peptides. **c,** Mass spectra of the peptide with highest uptake difference (residues 56-70). Almost no change in m/z ratio can be detected between peptides derived from non-deuterated SRA (black) and deuterated complex (blue) after 120 min, an indication that this region of SRA is shielded from deuterium uptake by ApoL1. The corresponding peptide in unbound SRA (red) shows rapid deuterium incorporation already detectable after 1 min. Peptide mapping was obtained by using non-deuterated samples in technical triplicates (n=3). Deuterated sample data was obtained in technical duplicates (n=2), panels **a** and **b**.

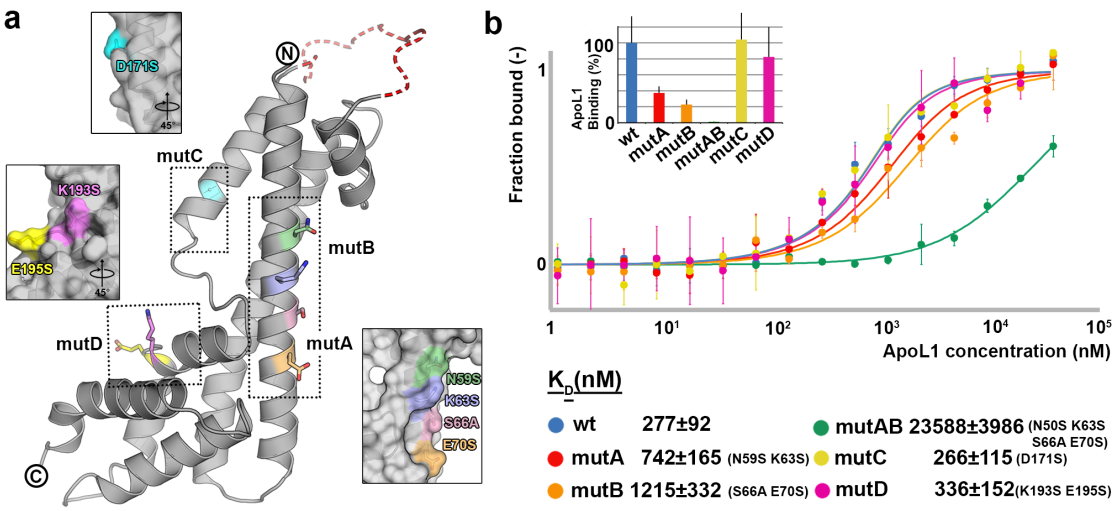

Figure 4. Mutational analysis of SRA binding to ApoL1. a, Four residues (N59, K63, S66 and E70) located in helix 1 of SRA were mutated in pairs (mutA and mutB) and these mutations were also combined in a quadruple mutant (mutAB). The side chains do not engage in intramolecular contacts, but are solvent-exposed and form a continuous stripe along helix 1, spanning four turns and covering an accessible surface area of 295 Å^2 (inset). In addition, mutC and mutD contained mutations in patches II and III, as identified by hydrogen-deuterium exchange. **b,** Affinity measurements of the binding of SRA and its mutants to ApoL1 determined using microscale thermophoresis. Dose-response curves show a significant reduction in binding affinity to ApoL1 for all SRA mutants in patches A and B. The combined effect of the four mutations in mutAB is a >80-fold decrease in affinity. The data shown are representative of three independent experiments (n=3) and the errors are calculated as standard deviation.

Supplementary Information

The structure of SRA and it implications for Human African Trypanosomiasis

Sebastian Zoll[a], Harriet Lane-Serff[a], Shahid Mehmood[b], Jonathan Schneider[a], Carol V. Robinson[b], Mark Carrington[c] and Matthew K. Higgins[a]

[a] Department of Biochemistry, South Parks Road, University of Oxford, OX1 3QU

[b] Physical and Theoretical Chemistry Laboratory, University of Oxford, South 32 Parks, OX1 3QZ, Oxford, UK

[c] Department of Biochemistry, Tennis Court Road, University of Cambridge, CB2 1QW

Construct	Residues	Expression	Crystallisation	Description
SRA S1	33-248	yes	No crystals formed	
SRA S2	33-261	yes	Diffraction to 6 Å	
SRA S2 short loop	33-141; 160-261	yes	No crystals formed	Loop between helix 2 and 3 truncated and substituted with sequence QGSTSGGGTTT
SRA S3	33-275	yes	No crystals formed	
SRA S4	33-283	yes, but C-terminal degradation	No crystals formed	
SRA S2 Entropy mutant	33-261	no	N/A	Surface entropy reducing mutations Q142A, K144A, E146A, K148A, E173A, K174A, Q174A, K206A, K207A, K210A, K240A, E241A, K242A
SRA S2 T4-L	33-261	no	N/A	T4 lysozyme insertion between helix 1 and 2

Supplementary Table 1. SRA constructs assessed for expression and crystallisation properties. Only variant S2 formed crystals, but these were not sufficiently ordered to allow structure determination. This construct was chosen for further trials in complex with Fab fragments. Residue numbers refer to the full polypeptide including the N-terminal signal sequence, which is predicted to be residues 1-32.

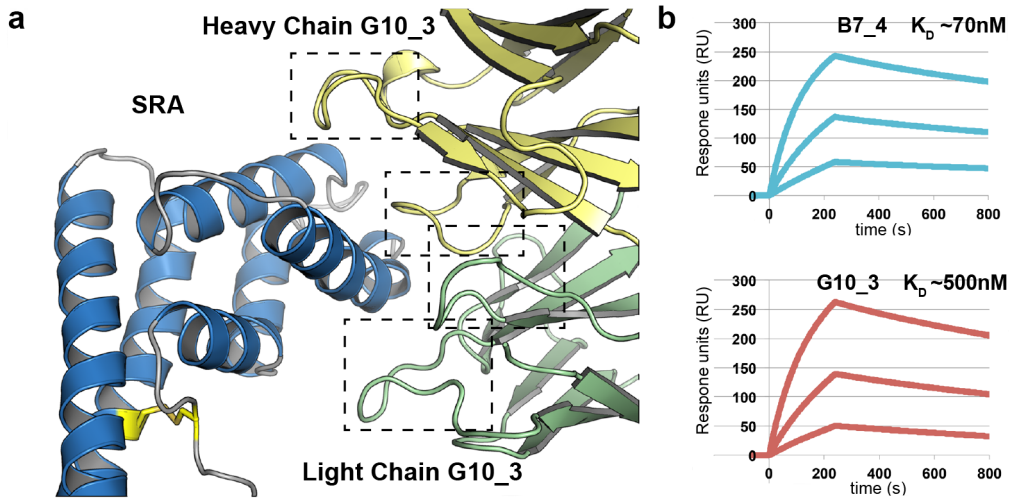

Supplementary Figure 1. Binding of SRA to monoclonal antibodies B7_4 and G10_3. a, A close-up view of the interface between SRA and the Fab fragment of monoclonal antibody G10_3. The hyper-variable loops of G10_3 contact helices 7 and 8 of SRA in the membrane-proximal region of the molecule. **b,** Surface plasmon resonance sensorgrams show binding of SRA to antibodies B7_4 and G10_3 that have been coupled to a CM5 chip. Sensorgram lines correspond to SRA concentrations of 250nM, 125nM and 62.5nM and each data set shown are from a single concentration series (n=1).

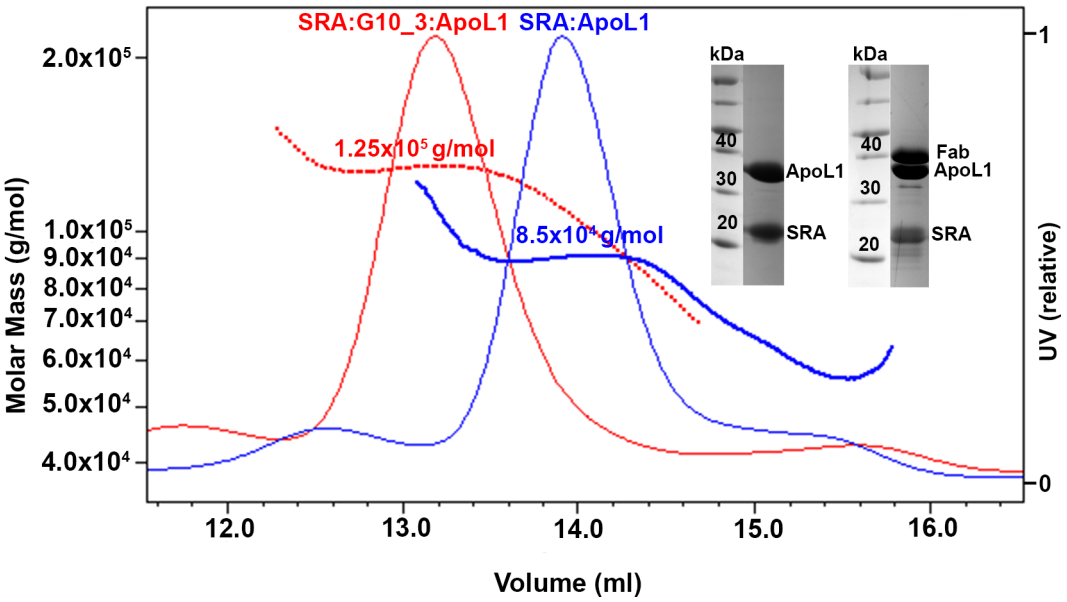

Supplementary Figure 2. Determination of the molar masses of SRA:ApoL1 and SRA:G10_3:ApoL1 by size exclusion chromatography multi-angle laser light scattering (SEC-MALLS). Both complexes remain intact during SEC, demonstrating the formation of stable, high-affinity interactions. The Fab fragment from G10_3 binds to pre-assembled SRA:ApoL1 complex, indicating that the G10_3 epitope on SRA does not overlap with the ApoL1 binding site. The mass determined for the SRA:ApoL1 complex matches the expected mass of 62 kDa together with the addition of ~25 kDa of dodecylmaltoside. The SRA:G10_3:ApoLI complex is ~40 kDa larger, matching the expected addition of 48 kDa for the Fab-fragment. SEC was performed on a Superdex 200 10/300 column with a running buffer of 20 mM citric acid pH 4.8, 150 mM NaCl and 0.02% DDM. This matches the pH expected in the lysosomal-endosomal compartment. Each dataset is from a single measurement (n=1).

Data collection	
Space group	$P2_1$
Cell dimensions (Å)	127.6 103.6 150.6
Angles (°)	90.0 114.6 90.0
Wavelength (Å)	0.97625
Resolution (Å)	47.3-2.3 (2.38-2.30)
R_{sym}* (%)	7.6 (51.4.)
R_{meas}** (%)	9.1 (61.1)
CC (1/2) (%)	99.7 (21.8)
I/σI	9.5 (2.7)
Completeness (%)	99.4 (99.4)
Redundancy	3.4 (3.4)
Total refelections	1062551 (77093)
Unique reflections	310049 (22960)

Refinement	
Resolution (Å)	48.4-2.3
R_{work}/R_{free}*** (%)	19.1/22.0
Solvent content (%)	61.0
Number of atoms	
Protein	18685
Water	542
B-factors (Å^2)	
SRA	
Chain A	106.9
Chain D	123.8
Chain G	109.9
Chain J	107.7
Fab heavy chain	
Chain B	62.5
Chain E	57.8
Chain H	55.9
Chain K	56.8
Fab light chain	
Chain C	54.9
Chain F	54.2
Chain I	50.8
Chain L	62.2
Water	55.6
r.m.s deviations	
Bond lengths (Å)	0.01
Bond angles (°)	1.03
Ramachandran plot (%)	
Most favored region	97.1
Additionally allowed region	2.9

Supplementary Table 2. **Data collection and structure refinement statistics.** Values in parentheses correspond to the highest resolution bin.

* $R_{sym} = \Sigma \mid I - < I > \mid / \Sigma I$
** R_{meas}= Redundancy independent R_{sym}
*** $R_{work} = \Sigma \mid \mid F_{obs}(hkl) \mid - \mid F_{calc}(hkl) \mid \mid / \Sigma \mid F_{obs}(hkl)$
*** R_{free}= Cross-validation R-factor for 5% of test set of reflections omitted from model refinement
r.m.s. root mean square

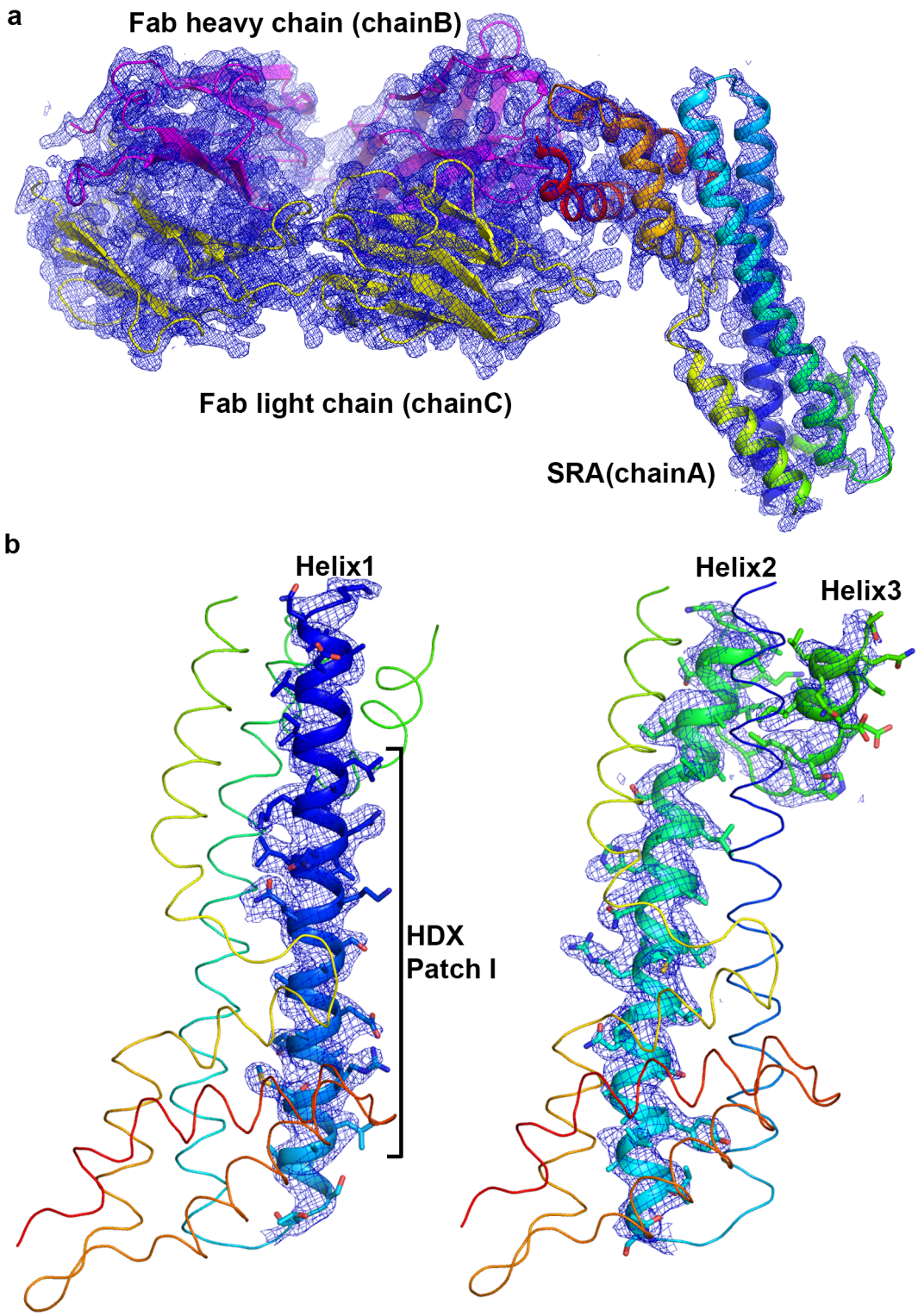

Supplementary Figure 3. 2Fo-Fc electron density maps contoured at 1σ. a, View of the SRA:G10_3 complex . Chains A (SRA, rainbow), B (heavy chain, magenta) and C (light chain, yellow) display the best electron density and the lowest B-factors of the four copies of the complex in the asymmetric unit of the crystal. **b**, Electron density for helix 1 (left) and Helix 2 and 3 (right) of SRA chain A. The model is coloured as a rainbow from blue (N-terminus) to red (C-terminus). The disordered loop 3 is omitted for clarity.

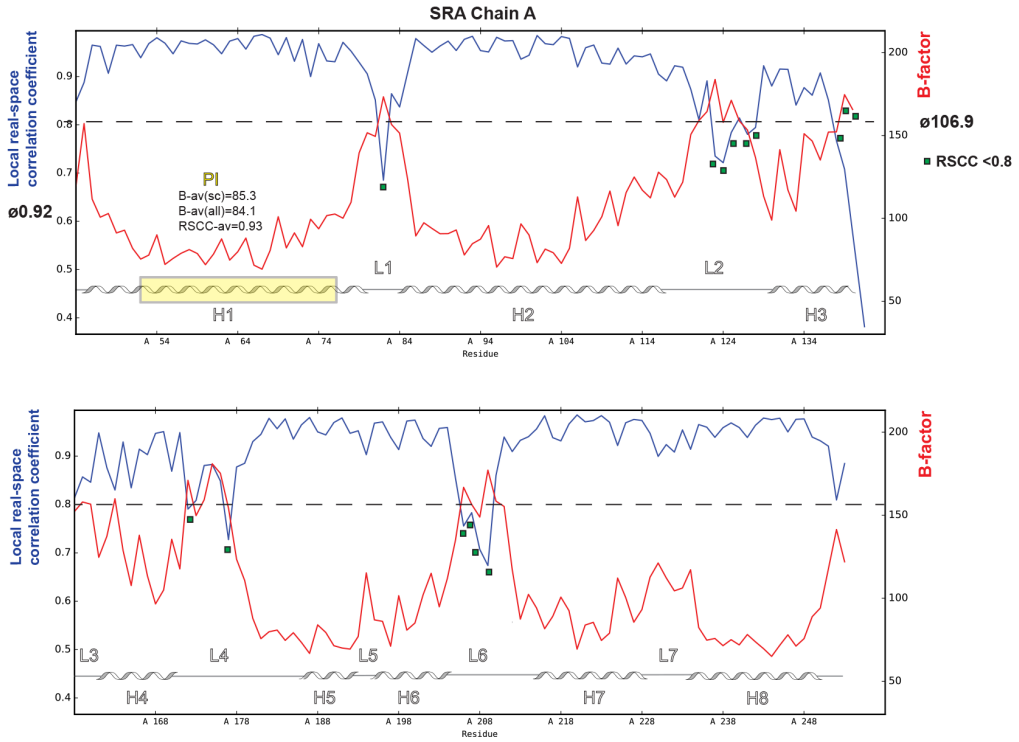

Supplementary Figure 4. B-factor and real space correlation coefficient (RSCC) plot for SRA chain A. The positions of secondary structure elements are indicated. Residues with an RSCC of <0.8 are marked with a green square and are present only in the loop regions. RSCC and B-factor averages are displayed next to the respective axis. The position of HDX patch I is marked with a yellow rectangle. The B-factor average for this region (all atoms and side chains) as well as the RSCC average is indicated.

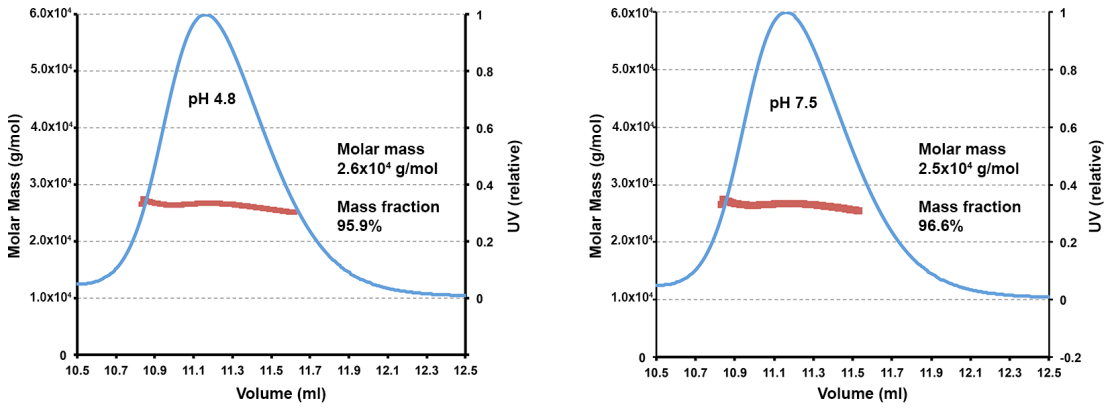

Supplementary Figure 5. Molar mass determination of SRA at pH 4.8 and 7.5 using SEC-MALLS. SEC-MALLS analysis confirms that SRA is a monomer in solution at acidic pH (20 mM citric acid pH 4.8, 150 mM NaCl, left panel) as well as at neutral pH (20 mM Hepes pH 7.5, 150 mM NaCl, right panel). SEC was performed on a Superdex 75 10/300 column. Each dataset is from a single measurement (n=1).

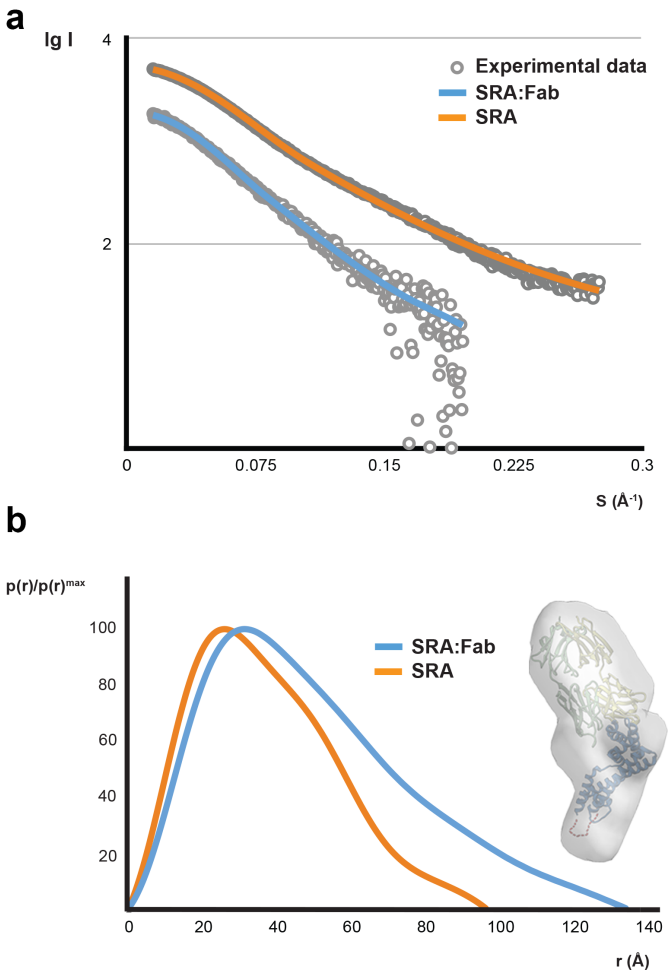

Supplementary Figure 6. Analysis by small angle X-ray scattering of SRA and the SRA:G10_3 Fab complex. **a,** Theoretical scattering curves calculated from *ab initio* models are superimposed on the experimental data. **b,** Normalised pair distance distribution function of SRA and the SRA:G10_3 Fab complex and an *ab initio* model of SRA:G10_3 Fab with the crystal structure docked into the molecular envelope. The data shown are from a single concentration series of six measurements (n=1).

	R_g (Å)[a]	R_g (Å)[b]	D_{max} (Å)	Volume (nm^3)[c]	Volume (nm^3)[d]	MW_{app} (kDa)[e]	MW_{exp} (kDa)	χ^2
SRA:Fab	38.7±2.9	38.3±1.3	134	137.1	126.7	71.4	73.1	1.04
SRA	28.8±0.2	28.4±0.3	96	59.4	55.2	34.3	24.5	1.07

[a] radius of gyration calculated using Gunier approximation
[b] radius of gyration calculated using indirect fourier transformation
[c] Porod volume calculated using Gunier approximation
[d] Porod volume calculated using indirect fourier transformation
[e] Molecular weight estimation using a method by Rambo *et al.*

Supplementary Table 3. Overall parameters for SAXS data. The fit of the *ab initio* models generated by DAMMIN to the experimental data is indicated by the χ^2 values.

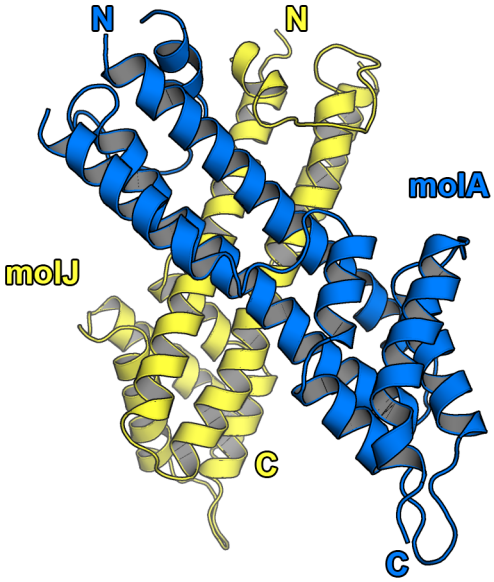

Supplementary Figure 7. SRA molecules form a crystallographic dimer. Within the crystal, SRA molecules make contacts to symmetry-related molecules in the neighbouring asymmetric unit resulting in an X-shaped crystallographic dimer.

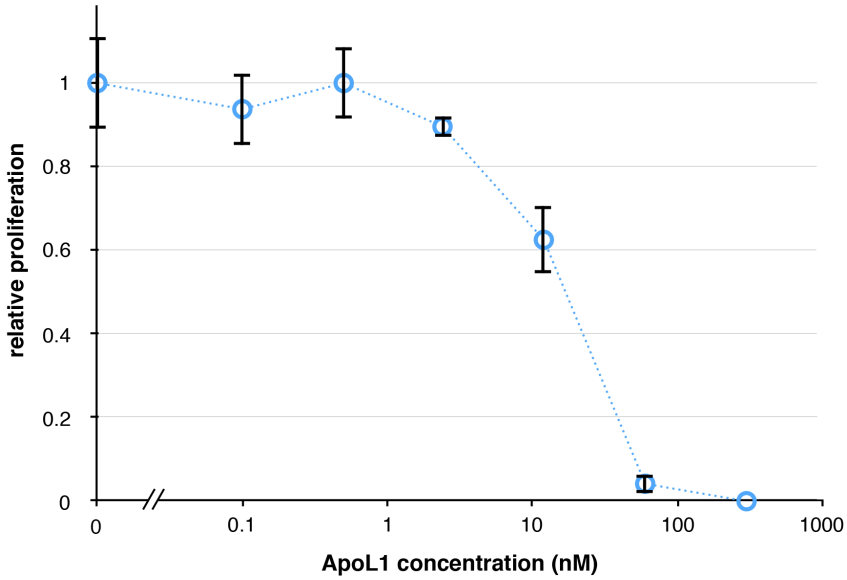

Supplementary Figure 8. Assessment of recombinant ApoLI in a trypanosome killing assay. The degree of proliferation of *T. b. brucei* after 24h in culture in the presence of different concentrations of recombinant ApoL1 (where 1 = 5-fold increase in cell density). Recombinant ApoL1 kills trypanosome with an EC_{50} of approx. 10 nM. Measurements are technical triplicates (n=3) and error bars are standard deviations.

B-factors Helix I HDX Patch I		
	Average B-factor all atoms	Average B-factor side chain
A 55 LEU	90.0	93.2
A 56 ALA	72.2	76.2
A 57 LYS	75.8	80.1
A 58 ILE	78.9	79.8
A 59 ASN	81.1	79.9
A 60 ASN	78.8	82.4
A 61 LEU	72.0	70.4
A 62 ILE	78.4	79.5
A 63 LYS	87.6	95.9
A 64 GLN	74.8	75.0
A 65 VAL	79.9	83.1
A 66 SER	88.1	96.7
A 67 ALA	71.7	65.8
A 68 ALA	69.3	63.5
A 69 THR	80.7	87.6
A 70 GLU	101.0	113.1
A 71 ALA	82.2	74.0
A 72 GLU	91.2	98.0
A 73 ALA	82.9	62.8
A 74 ARG	99.5	104.8
A 75 MET	93.7	90.9
A 76 THR	101.7	104.1
A 77 LEU	102.6	106.2
ø	**84.1**	**85.3**

Supplementary Table 4. B-factors for residues of Helix I HDX Patch I. Average B-factors are shown for all atoms as well as side chains only.

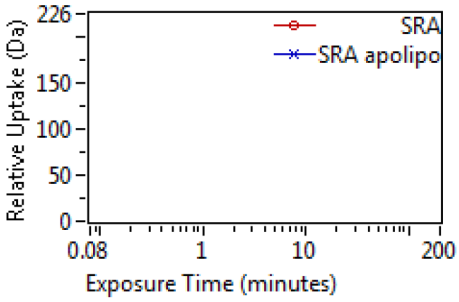
Relative Uptake (Da)
226
150
100
50
0
SRA
SRA apolipo
0.08
1
10
200
Exposure Time (minutes)

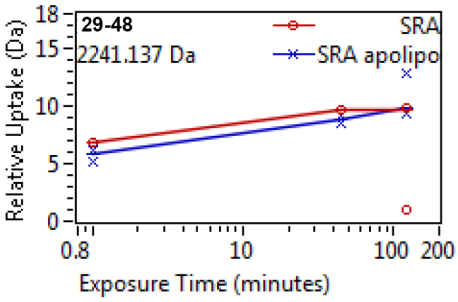
Relative Uptake (Da)
18
15
10
5
0
29-48
2241.137 Da
SRA
SRA apolipo
0.8
10
100
200
Exposure Time (minutes)

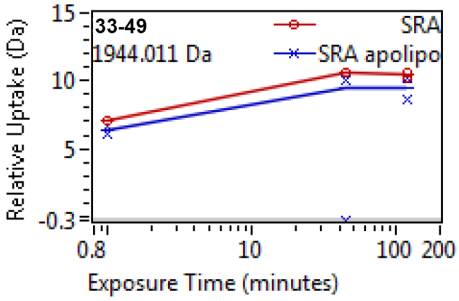
Relative Uptake (Da)
15
10
5
-0.3
33-49
1944.011 Da
SRA
SRA apolipo
0.8
10
100
200
Exposure Time (minutes)

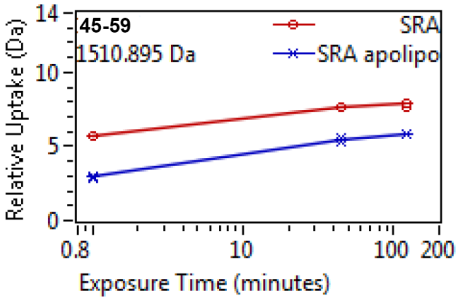
Relative Uptake (Da)
14
10
5
0
45-59
1510.895 Da
SRA
SRA apolipo
0.8
10
100
200
Exposure Time (minutes)

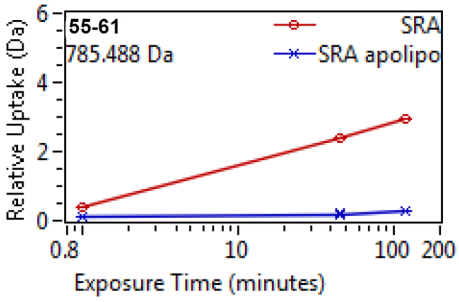
Relative Uptake (Da)
6
4
2
0
55-61
785.488 Da
SRA
SRA apolipo
0.8
10
100
200
Exposure Time (minutes)

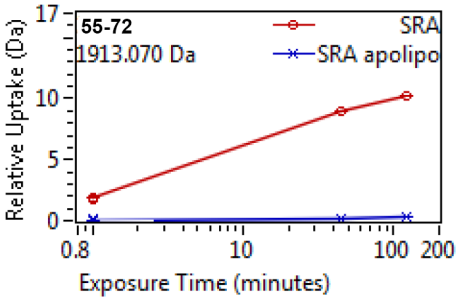
Relative Uptake (Da)
17
10
5
0
55-72
1913.070 Da
SRA
SRA apolipo
0.8
10
100
200
Exposure Time (minutes)

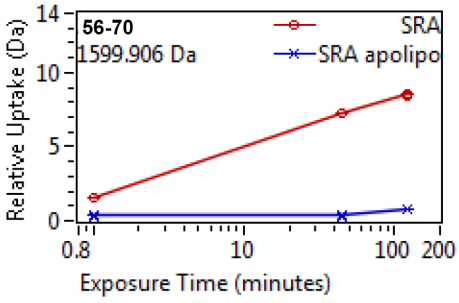
Relative Uptake (Da)
14
10
5
0
56-70
1599.906 Da
SRA
SRA apolipo
0.8
10
100
200
Exposure Time (minutes)

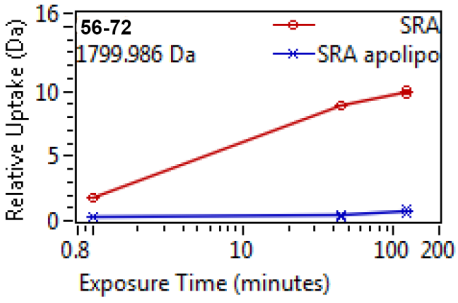
Relative Uptake (Da)
16
10
5
0
56-72
1799.986 Da
SRA
SRA apolipo
0.8
10
100
200
Exposure Time (minutes)

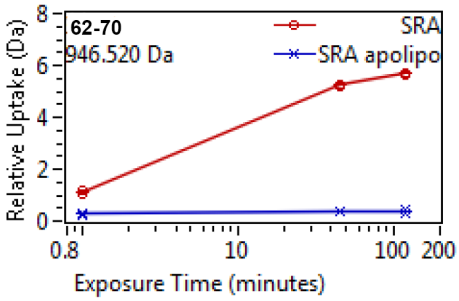
Relative Uptake (Da)
8
6
4
2
0
62-70
946.520 Da
SRA
SRA apolipo
0.8
10
100
200
Exposure Time (minutes)

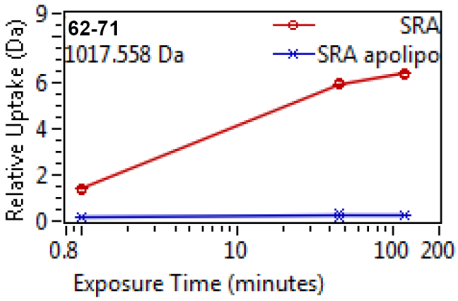
Relative Uptake (Da)
9
6
4
2
0
62-71
1017.558 Da
SRA
SRA apolipo
0.8
10
100
200
Exposure Time (minutes)

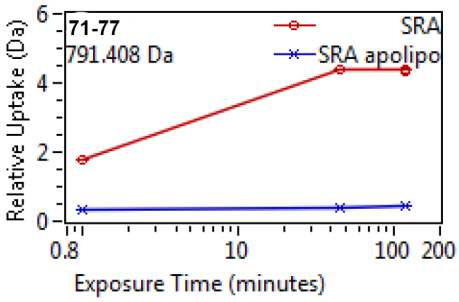
Relative Uptake (Da)
6
4
2
0
71-77
791.408 Da
SRA
SRA apolipo
0.8
10
100
200
Exposure Time (minutes)

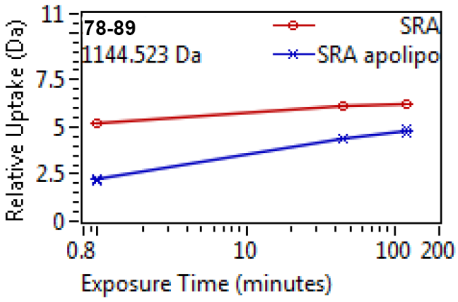
Relative Uptake (Da)
11
7.5
5
2.5
0
78-89
1144.523 Da
SRA
SRA apolipo
0.8
10
100
200
Exposure Time (minutes)

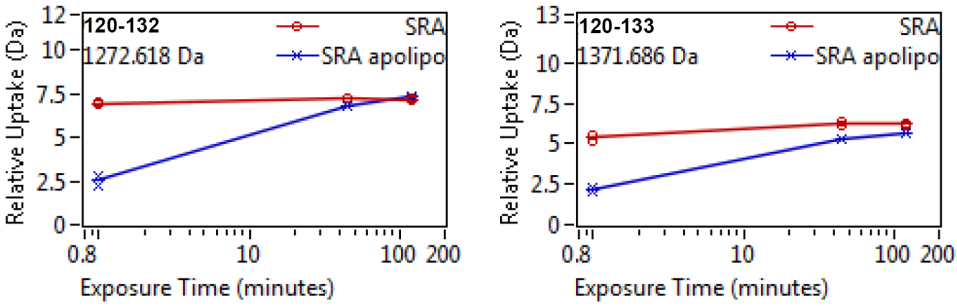
120-132
1272.618 Da
SRA
SRA apolipo
Relative Uptake (Da)
Exposure Time (minutes)

120-133
1371.686 Da
SRA
SRA apolipo
Relative Uptake (Da)
Exposure Time (minutes)

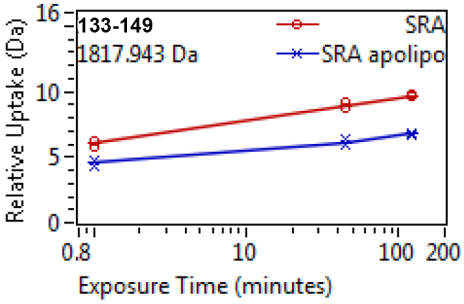
133-149
1817.943 Da
SRA
SRA apolipo
Relative Uptake (Da)
Exposure Time (minutes)

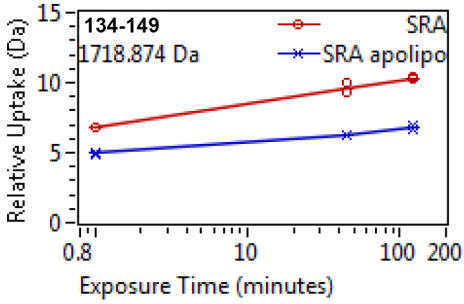
134-149
1718.874 Da
SRA
SRA apolipo
Relative Uptake (Da)
Exposure Time (minutes)

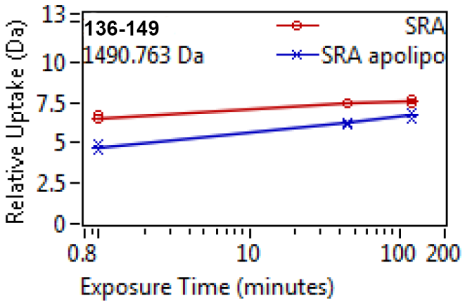
136-149
1490.763 Da
SRA
SRA apolipo
Relative Uptake (Da)
Exposure Time (minutes)

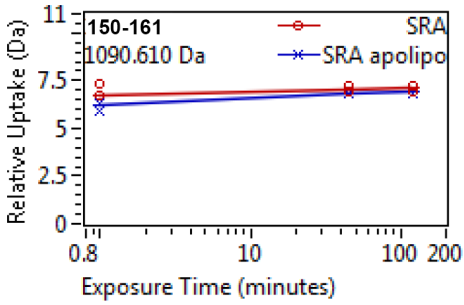
150-161
1090.610 Da
SRA
SRA apolipo
Relative Uptake (Da)
Exposure Time (minutes)

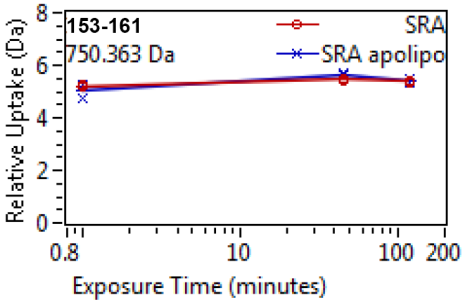
153-161
750.363 Da
SRA
SRA apolipo
Relative Uptake (Da)
Exposure Time (minutes)

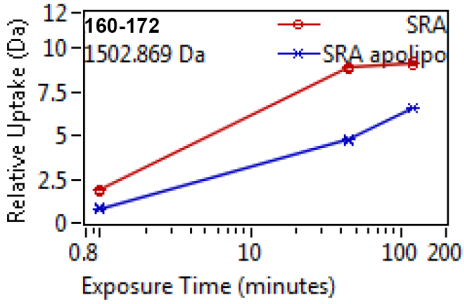
160-172
1502.869 Da
SRA
SRA apolipo
Relative Uptake (Da)
Exposure Time (minutes)

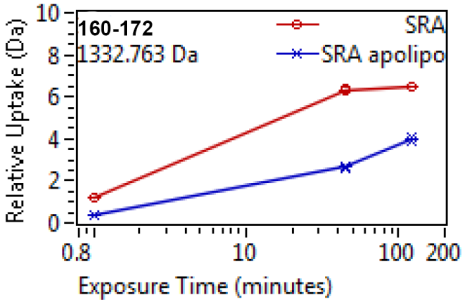
160-172
1332.763 Da
SRA
SRA apolipo
Relative Uptake (Da)
Exposure Time (minutes)

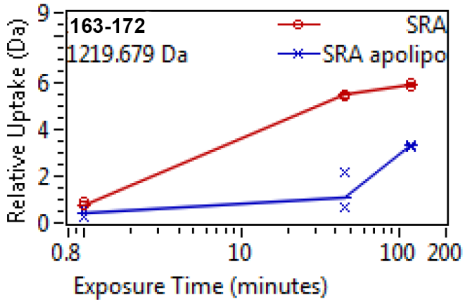
163-172
1219.679 Da
SRA
SRA apolipo
Relative Uptake (Da)
Exposure Time (minutes)

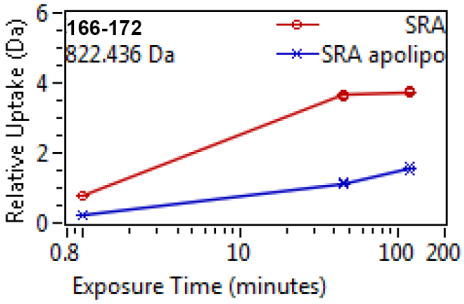
166-172
822.436 Da
SRA
SRA apolipo
Relative Uptake (Da)
Exposure Time (minutes)

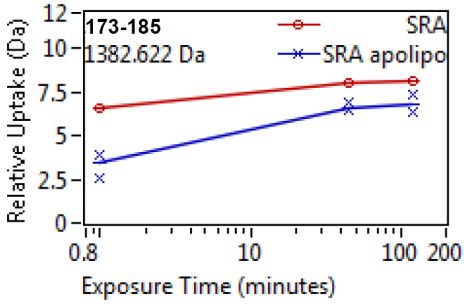
173-185
1382.622 Da
SRA
SRA apolipo
Relative Uptake (Da)
Exposure Time (minutes)

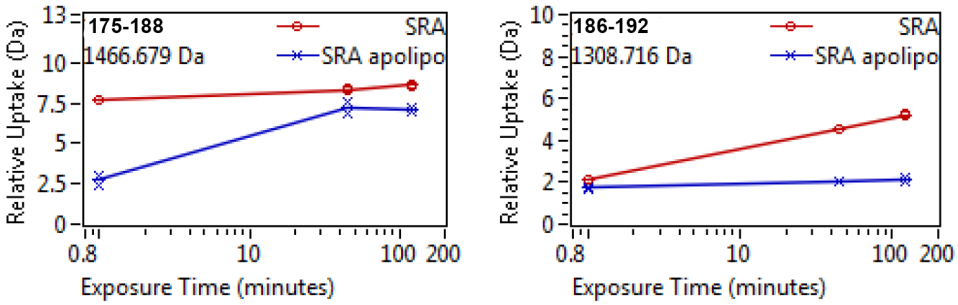
175-188
1466.679 Da
SRA
SRA apolipo
Relative Uptake (Da)
Exposure Time (minutes)

186-192
1308.716 Da
SRA
SRA apolipo
Relative Uptake (Da)
Exposure Time (minutes)

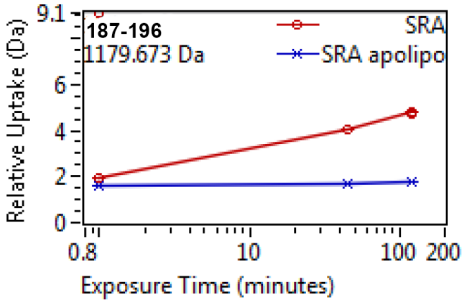
187-196
1179.673 Da
SRA
SRA apolipo
Relative Uptake (Da)
Exposure Time (minutes)

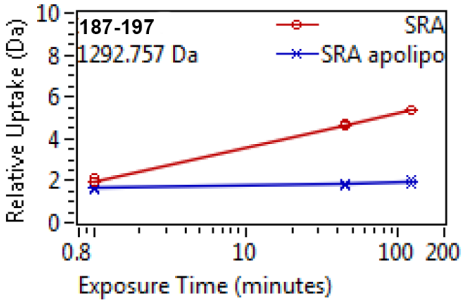
187-197
1292.757 Da
SRA
SRA apolipo
Relative Uptake (Da)
Exposure Time (minutes)

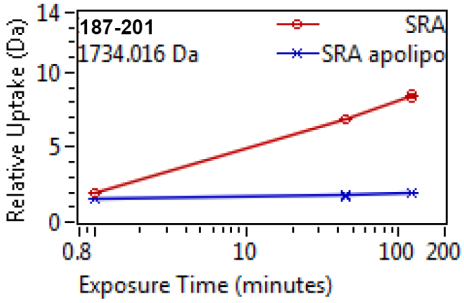
187-201
1734.016 Da
SRA
SRA apolipo
Relative Uptake (Da)
Exposure Time (minutes)

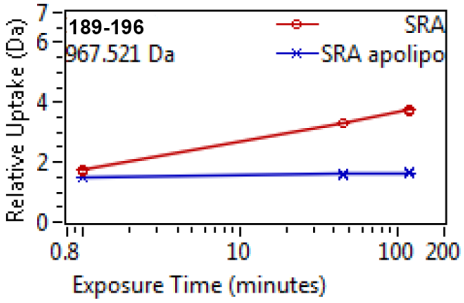
189-196
967.521 Da
SRA
SRA apolipo
Relative Uptake (Da)
Exposure Time (minutes)

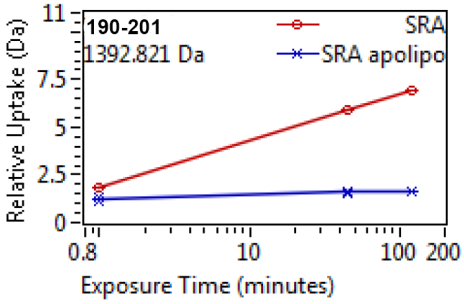
190-201
1392.821 Da
SRA
SRA apolipo
Relative Uptake (Da)
Exposure Time (minutes)

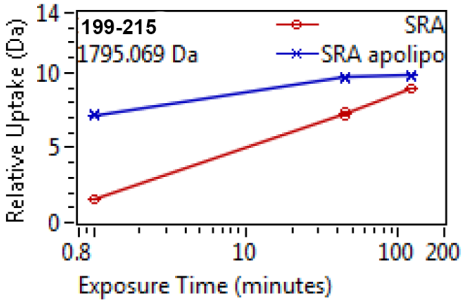
199-215
1795.069 Da
SRA
SRA apolipo
Relative Uptake (Da)
Exposure Time (minutes)

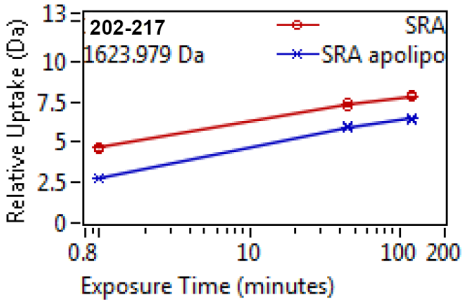
202-217
1623.979 Da
SRA
SRA apolipo
Relative Uptake (Da)
Exposure Time (minutes)

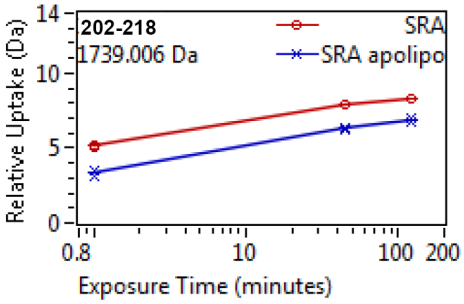
202-218
1739.006 Da
SRA
SRA apolipo
Relative Uptake (Da)
Exposure Time (minutes)

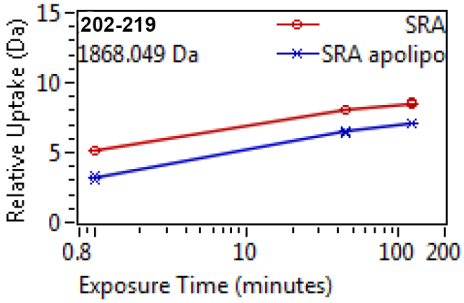
202-219
1868.049 Da
SRA
SRA apolipo
Relative Uptake (Da)
Exposure Time (minutes)

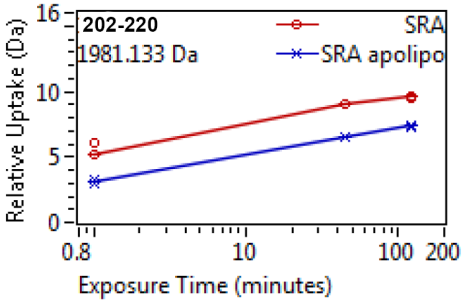
202-220
1981.133 Da
SRA
SRA apolipo
Relative Uptake (Da)
Exposure Time (minutes)

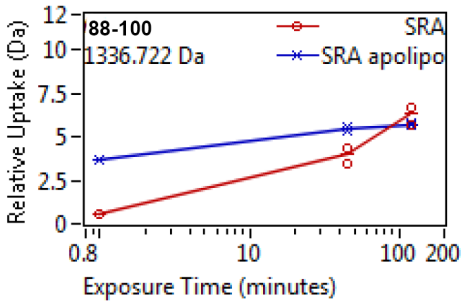
88-100
1336.722 Da
SRA
SRA apolipo
Relative Uptake (Da)
Exposure Time (minutes)

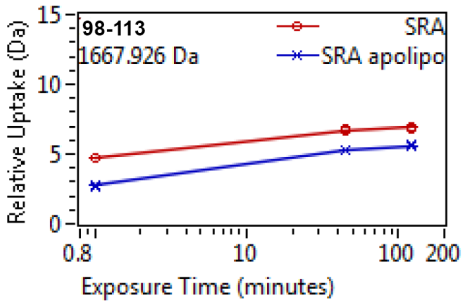
98-113
1667.926 Da
SRA
SRA apolipo
Relative Uptake (Da)
Exposure Time (minutes)

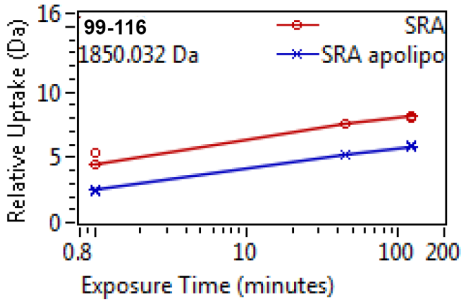
99-116
1850.032 Da
SRA
SRA apolipo
Relative Uptake (Da)
Exposure Time (minutes)

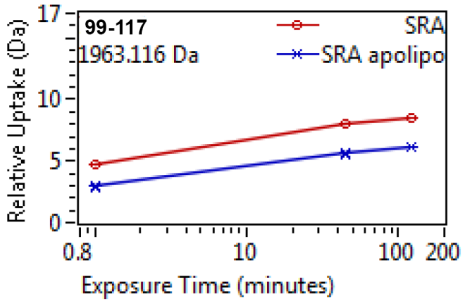
99-117
1963.116 Da
SRA
SRA apolipo
Relative Uptake (Da)
Exposure Time (minutes)

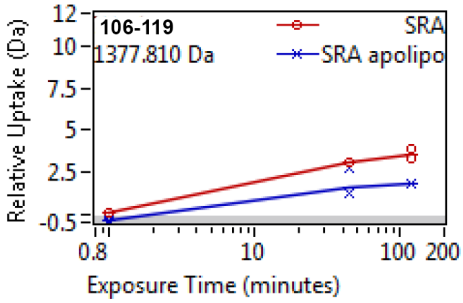
106-119
1377.810 Da
SRA
SRA apolipo
Relative Uptake (Da)
Exposure Time (minutes)

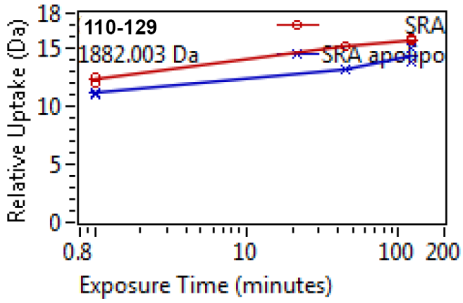
110-129
1882.003 Da
SRA
SRA apolipo
Relative Uptake (Da)
Exposure Time (minutes)

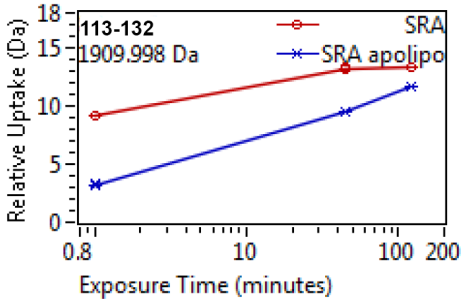
113-132
1909.998 Da
SRA
SRA apolipo
Relative Uptake (Da)
Exposure Time (minutes)

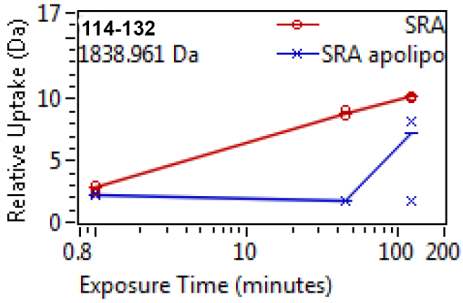
114-132
1838.961 Da
SRA
SRA apolipo
Relative Uptake (Da)
Exposure Time (minutes)

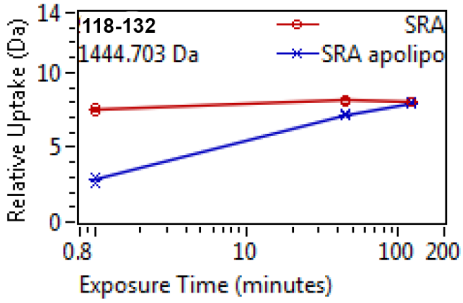
118-132
1444.703 Da
SRA
SRA apolipo
Relative Uptake (Da)
Exposure Time (minutes)

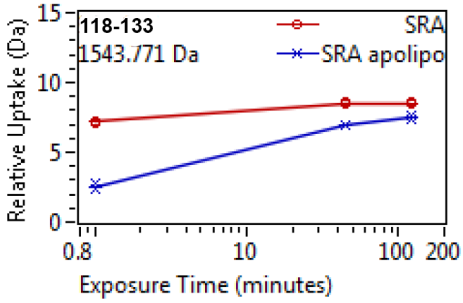
118-133
1543.771 Da
SRA
SRA apolipo
Relative Uptake (Da)
Exposure Time (minutes)

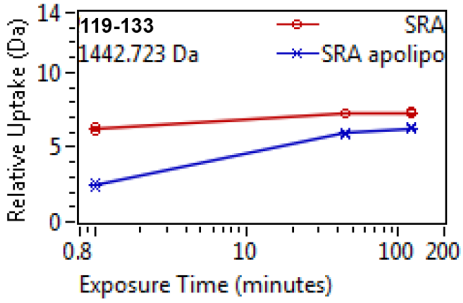
119-133
1442.723 Da
SRA
SRA apolipo
Relative Uptake (Da)
Exposure Time (minutes)

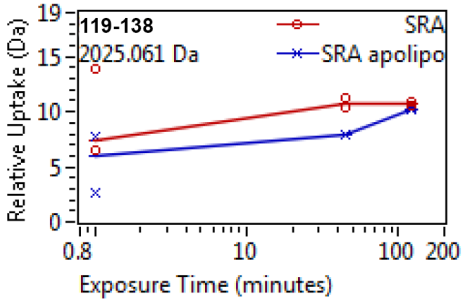
119-138
2025.061 Da
SRA
SRA apolipo
Relative Uptake (Da)
Exposure Time (minutes)

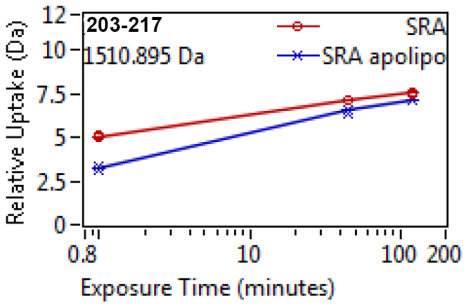
203-217
1510.895 Da
SRA
SRA apolipo
Relative Uptake (Da)
Exposure Time (minutes)

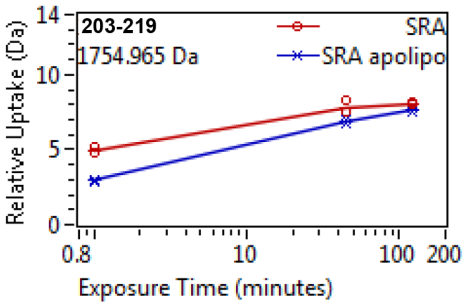
203-219
1754.965 Da
SRA
SRA apolipo
Relative Uptake (Da)
Exposure Time (minutes)

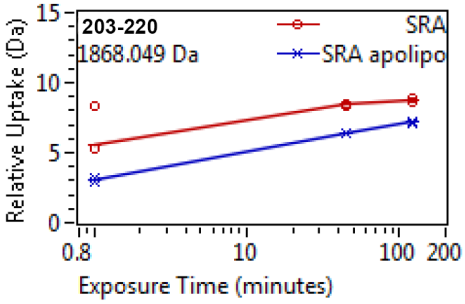
203-220
1868.049 Da
SRA
SRA apolipo
Relative Uptake (Da)
Exposure Time (minutes)

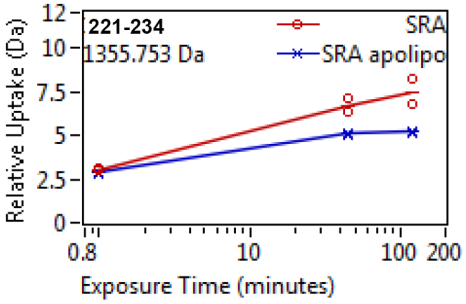
221-234
1355.753 Da
SRA
SRA apolipo
Relative Uptake (Da)
Exposure Time (minutes)

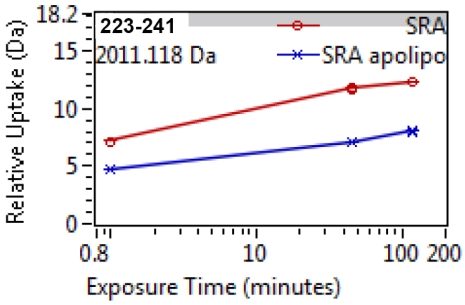
223-241
2011.118 Da
SRA
SRA apolipo
Relative Uptake (Da)
Exposure Time (minutes)

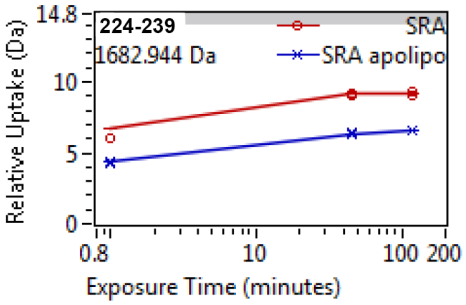
224-239
1682.944 Da
SRA
SRA apolipo
Relative Uptake (Da)
Exposure Time (minutes)

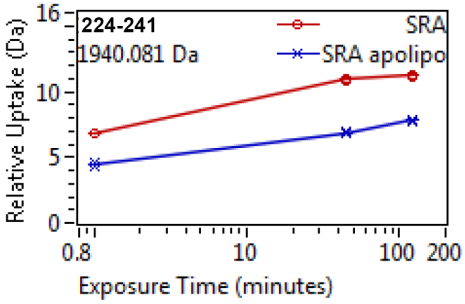
224-241
1940.081 Da
SRA
SRA apolipo
Relative Uptake (Da)
Exposure Time (minutes)

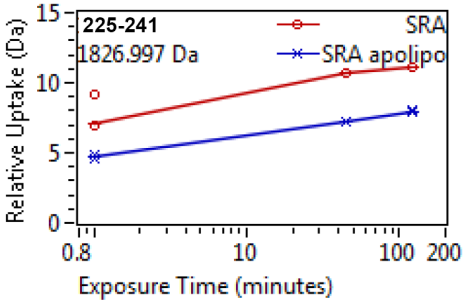
225-241
1826.997 Da
SRA
SRA apolipo
Relative Uptake (Da)
Exposure Time (minutes)

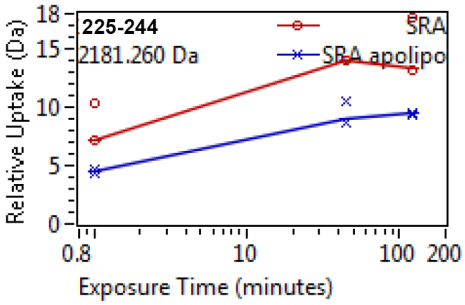
225-244
2181.260 Da
SRA
SRA apolipo
Relative Uptake (Da)
Exposure Time (minutes)

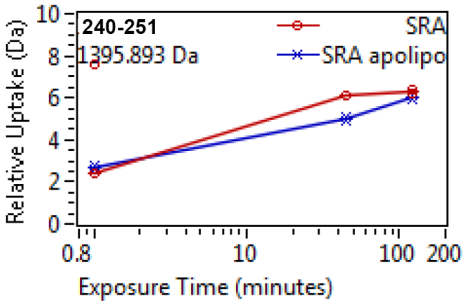
240-251
1395.893 Da
SRA
SRA apolipo
Relative Uptake (Da)
Exposure Time (minutes)

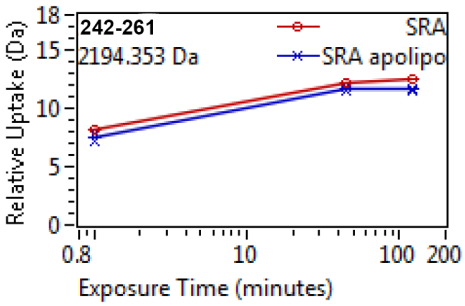
242-261
2194.353 Da
SRA
SRA apolipo
Relative Uptake (Da)
Exposure Time (minutes)

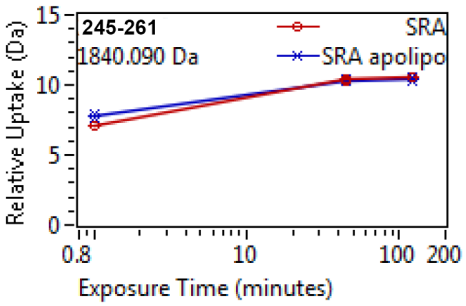
245-261
1840.090 Da
SRA
SRA apolipo
Relative Uptake (Da)
Exposure Time (minutes)

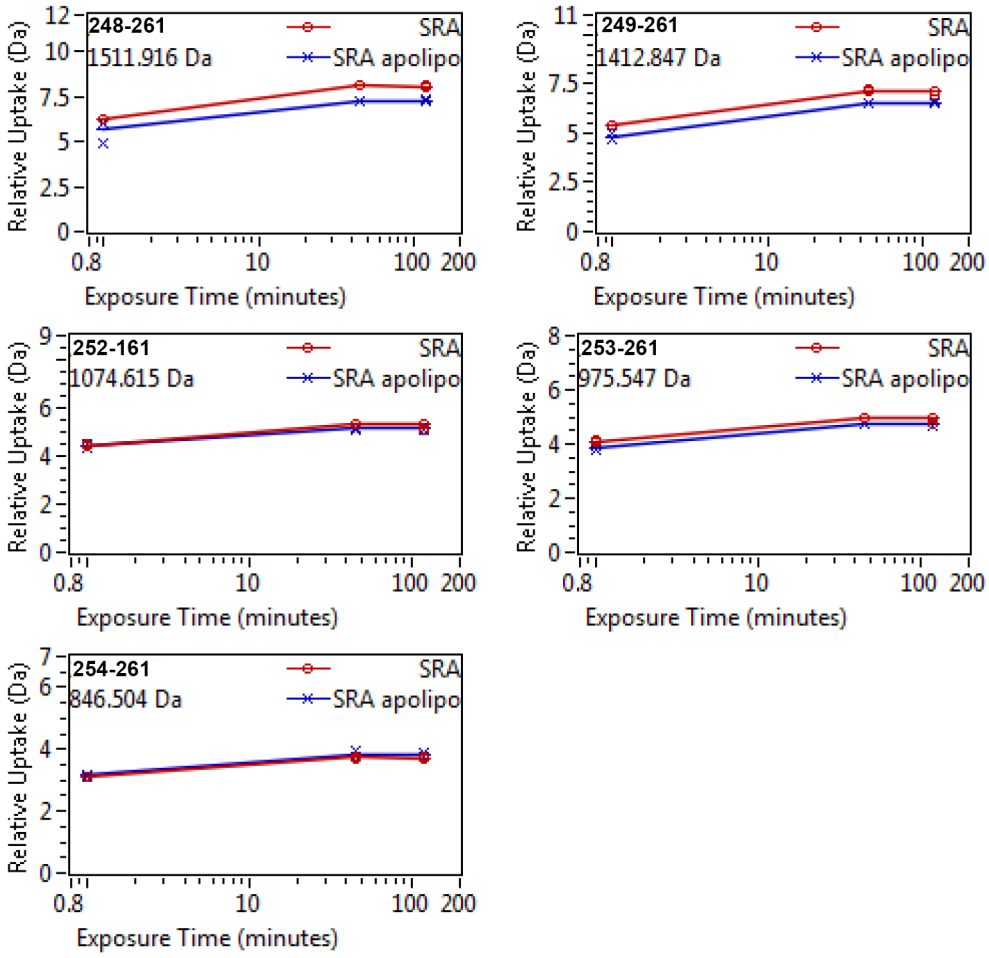

Supplementary Figure 9. Rates of relative deuterium uptake for peptides derived from SRA, analysed both alone and in complex with ApoL1. Peptide masses were determined after 1 min, 45 min and 120 min, revealing similar effects on exchange. The position of each peptide is indicated in the sequence of SRA. Plots were generated using DynamX (Waters). Non-deuterated samples were measured in technical triplicate (n=3), while deuterated samples were measured in technical duplicates (n=2).

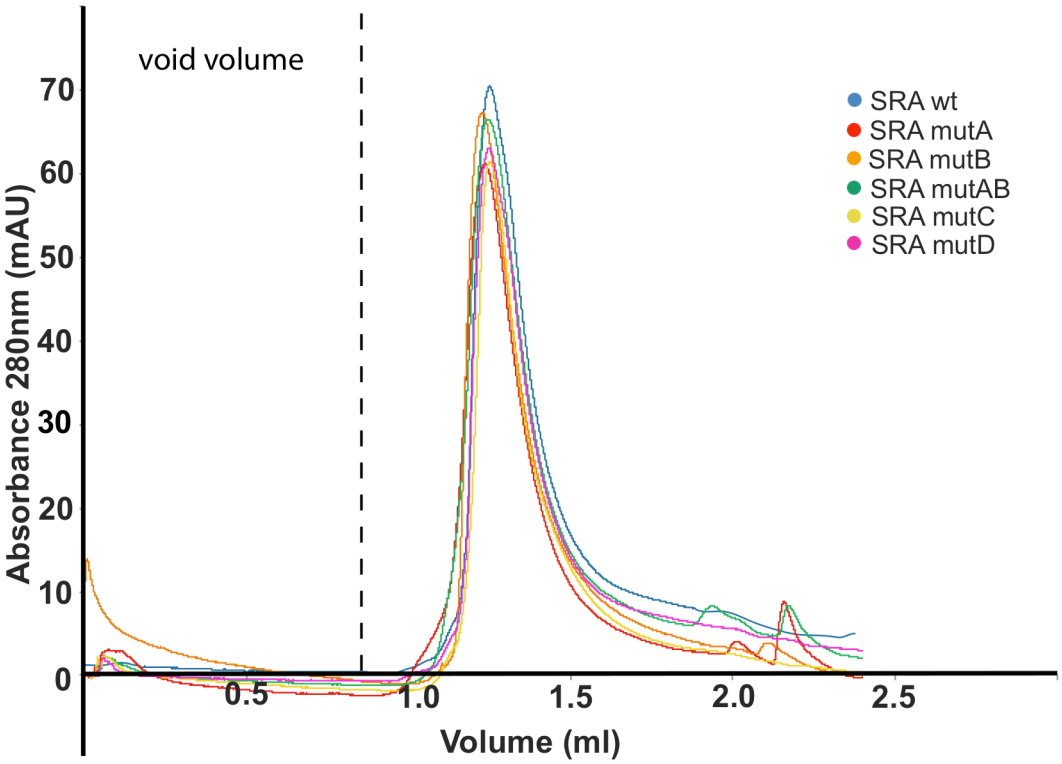

Supplementary Figure 10. Size exclusion chromatography of SRA and mutants. All mutants show identical retention times. SEC was performed on a Superdex 75 3.2/300 column using 20 mM citric acid pH 4.8, 150 mM NaCl. Each curve is from a single measurement (n=1).

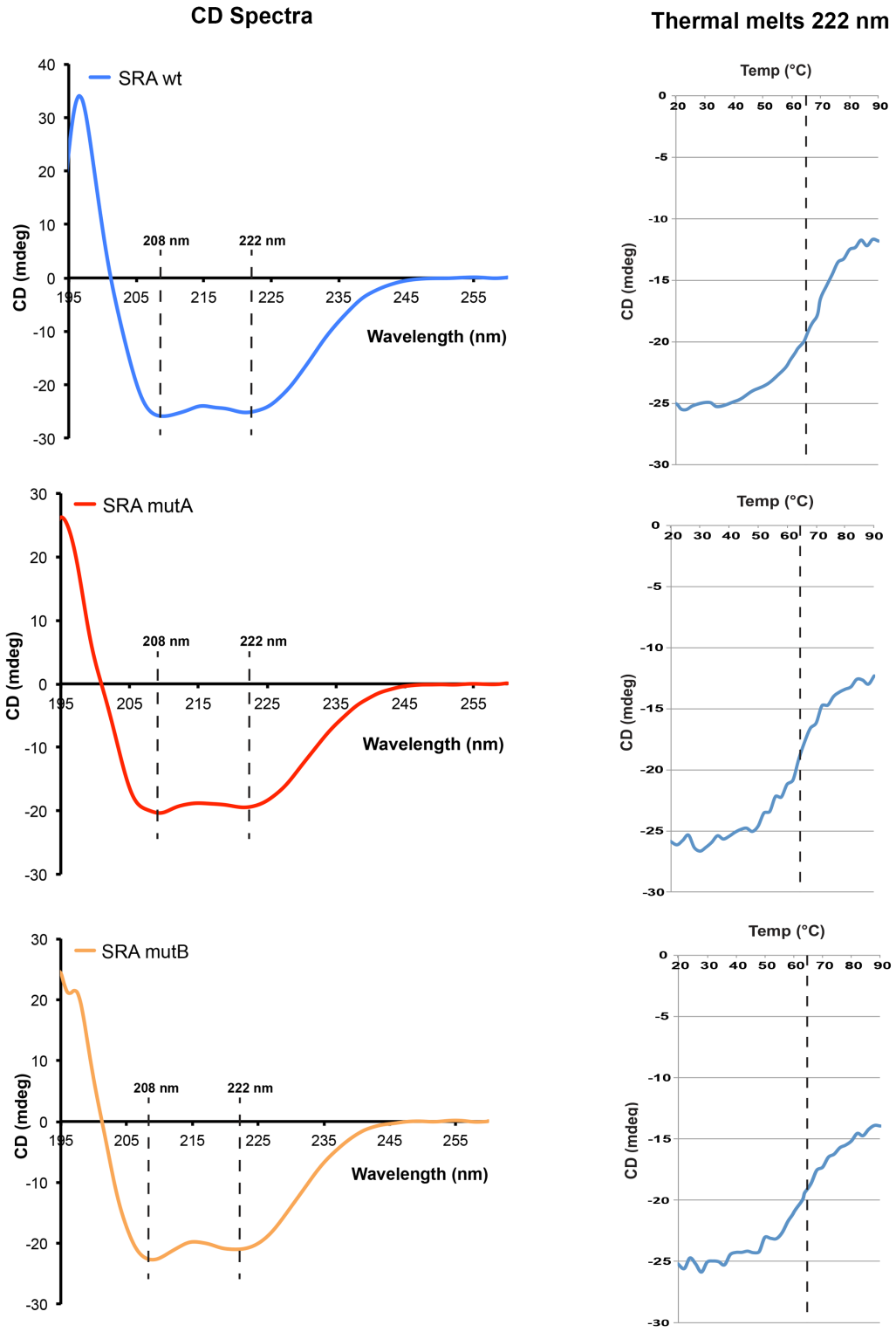
CD Spectra
Thermal melts 222 nm
SRA wt
SRA mutA
SRA mutB
CD (mdeg)
Wavelength (nm)
208 nm
222 nm
Temp (°C)

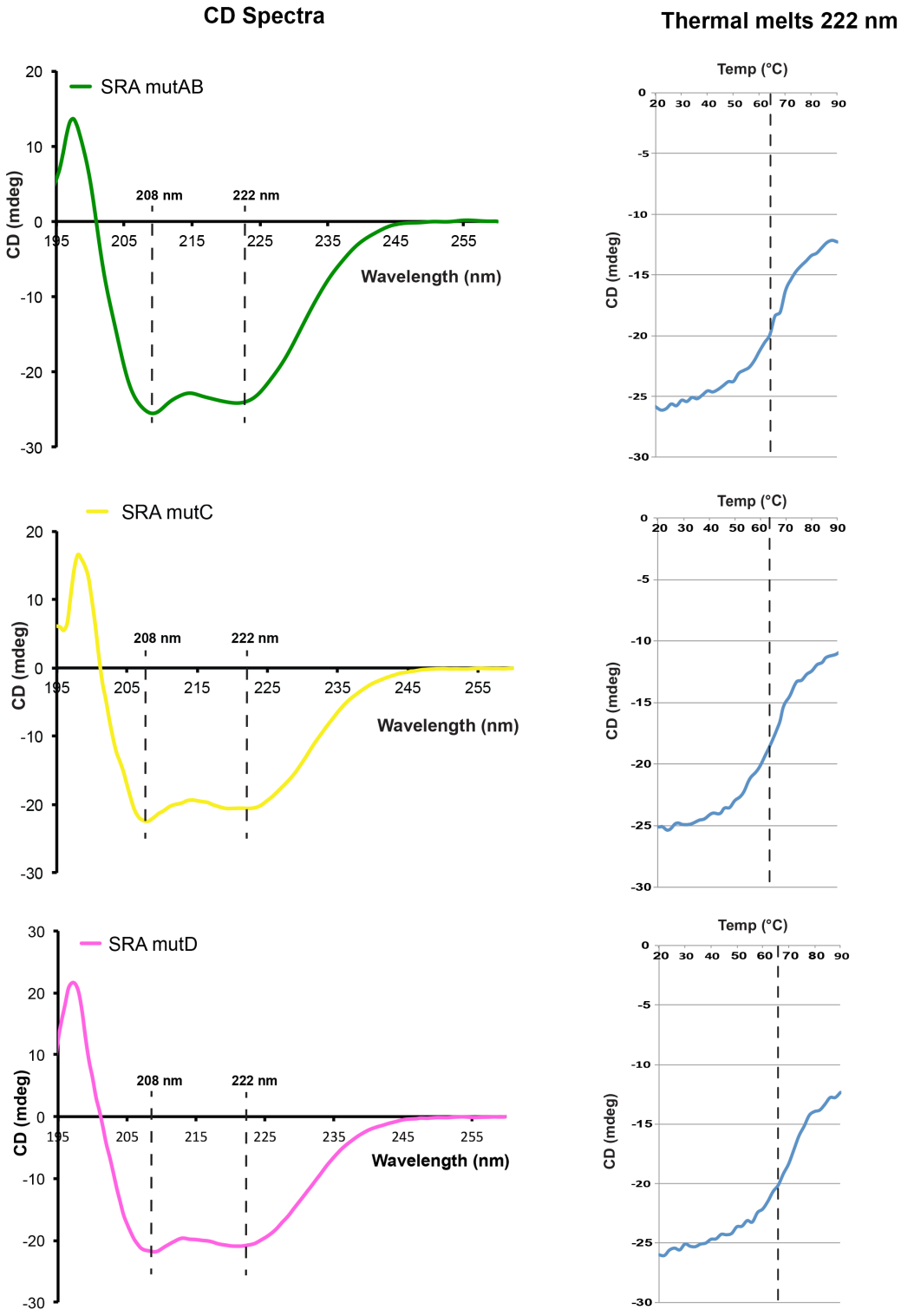

Supplementary Figure 11. Secondary structure analysis and thermal melts of SRA and mutants. Circular dichroism spectra of SRA and each of the mutants showed minima at 208 and 222 nm that are characteristic of alpha-helical proteins. Melting temperatures are approx. 65°C for all proteins. Each panel is from a single temperature series (n=1).

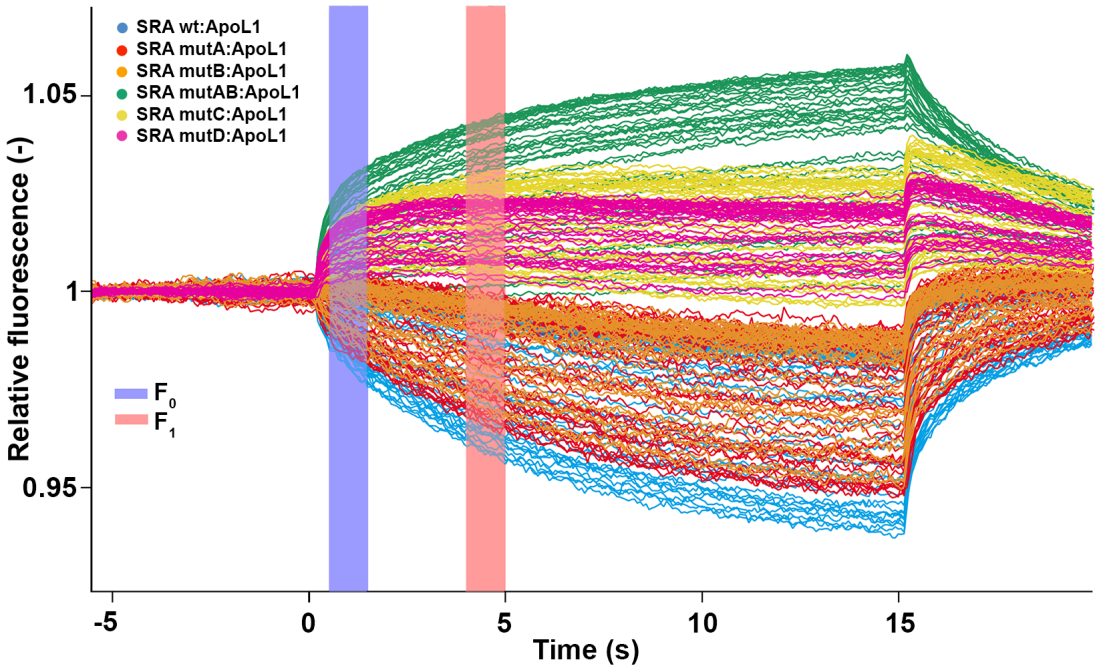

Supplementary Figure 12. Fluorescence time traces obtained by microscale thermophoresis for binding of ApoL1 to SRA and mutants. For signal analysis and calculation of dose-response curves the fluorescence after thermo-diffusion (F_1) was normalised to the fluorescence after the T-jump (F_0). All measurements were carried out in triplicate (n=3).

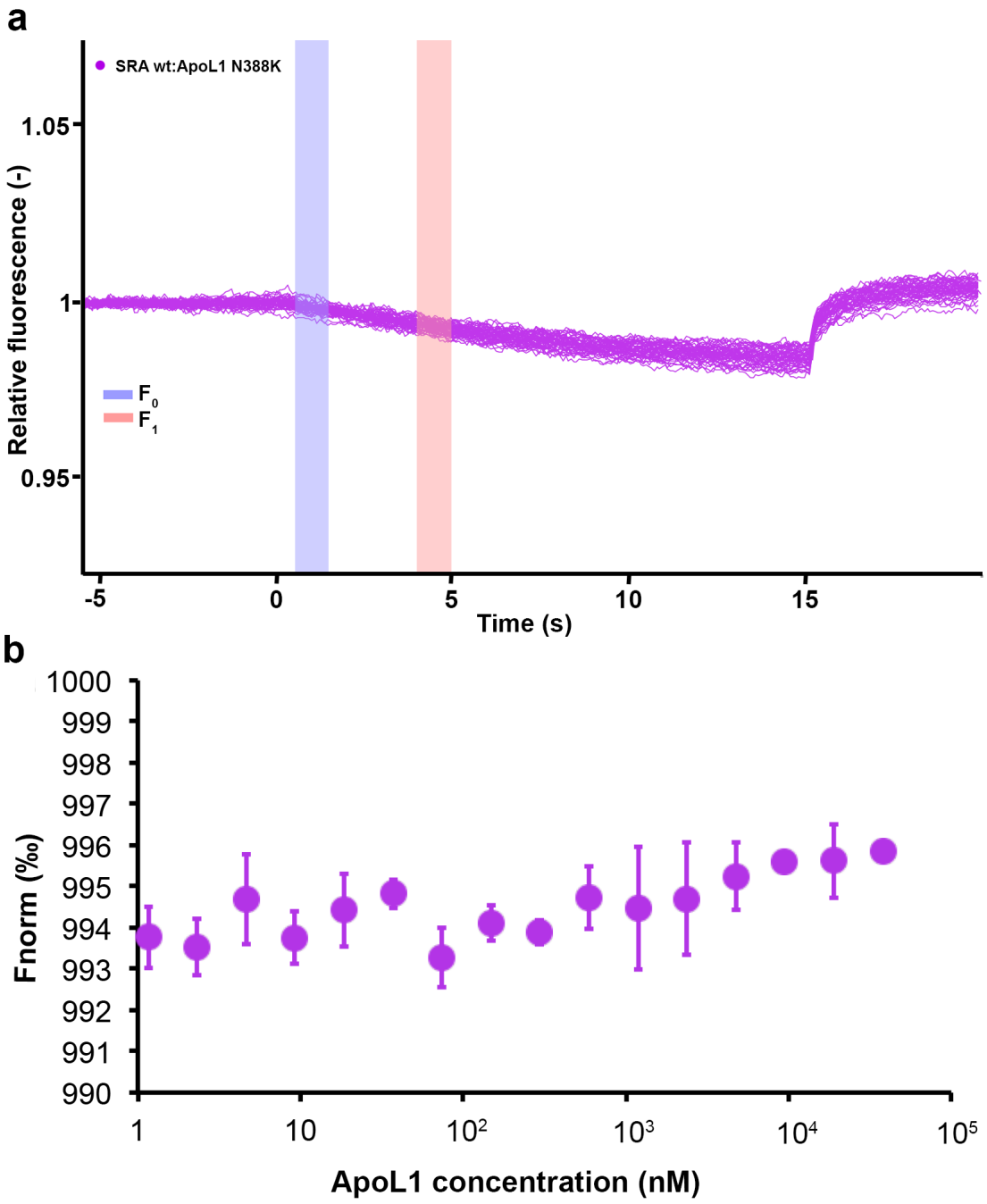

Supplementary Figure 13. Fluorescence time traces obtained by microscale thermophoresis for binding of SRA to ApoL1 N388K. a, Relative fluorescence plotted against time**.** For signal analysis the fluorescence after thermo-diffusion (F_1) was normalised to the fluorescence after the T-jump (F_0). **b,** Normalised fluorescence is plotted against ApoL1 N388K concentration. No dose-response curve could be fitted as no significant change in fluorescence with increasing ApoL1 concentration could be detected. All measurements were carried out in triplicates (n=3) and error bars are standard deviations.